SINGLE-MOLECULE DUAL-BEAM OPTICAL TRAP ANALYSIS OF PROTEIN STRUCTURE AND FUNCTION

Jongmin Sung,*,† Sivaraj Sivaramakrishnan,* Alexander R. Dunn,‡ and James A. Spudich*

Contents

Abstract

Optical trapping is one of the most powerful single-molecule techniques. We provide a practical guide to set up and use an optical trap, applied to the molecular motor myosin as an example. We focus primarily on studies of

* Department of Biochemistry, Stanford University School of Medicine, Stanford, California, USA
† Department of Applied Physics, Stanford University, Stanford, California, USA
‡ Department of Chemical Engineering, Stanford University, Stanford, California, USA

myosin function using a dual-beam optical trap, a protocol to build such a trap, and the experimental and data analysis protocols to utilize it.

1. INTRODUCTION

The development of the first dual–beam optical trap for single–molecule analysis was biology driven. The step size of the molecular motor myosin was in great dispute because *in vitro* motility assays to study myosin function examined the collective behavior of multiple motors (Harada *et al.*, 1987; Kron and Spudich, 1986; Uyeda *et al.*, 1990), and the step size of the individual myosin molecule was difficult to be certain of. In the early 1990s, it became clear that one needed to watch a single molecule of myosin go through one chemomechanical cycle and measure the step size directly. Finer *et al.* (1994) "simplified" the Kron and Spudich (1986) *in vitro* motility assay by developing the dual–beam optical trap system. Their study revealed a ~10 nm stroke size for muscle myosin II with ~5 pN forces generated by it. These results provided strong support for the lever arm model of myosin motion, also referred to as the swinging cross–bridge hypothesis (Huxley, 1969). Since 1994, the dual–beam optical trap has been used to study a variety of proteins at the single–molecule level (Bustamante *et al.*, 2007; Nishikawa *et al.*, 2007; Spudich *et al.*, 2007). Details of the early version of the dual–beam trap in our laboratory have been described elsewhere (Finer *et al.*, 1994; Rice *et al.*, 2003; Spudich *et al.*, 2007). Here, we describe a modern version of the dual–beam trap, which has primarily changed in terms of more highly developed individual components. We use myosin as the prototype molecule in describing the details of how to apply the trap to single–molecule analysis. The reader is referred to review papers for the recent advances in optical traps and their use (Berg-Sørensen and Flyvbjerg, 2004; Moffitt *et al.*, 2008; Neuman and Block, 2004; Perkins, 2009).

2. INSIGHTS INTO MYOSIN FUNCTION USING A DUAL-BEAM OPTICAL TRAP

Since the Finer *et al.* (1994) studies, the dual–beam optical trap has been widely used to study myosins. In translational research, for example, it was used to characterize changes in cardiac myosin II function caused by single–point mutations in the most common inherited heart disease, hypertrophic cardiomyopathy (Palmiter *et al.*, 1999, 2000). Optical trapping showed that the R403Q mutation in β–cardiac myosin, which results in sudden death, decreases myosin dwell time but does not alter stroke size or force–generating ability (Palmiter *et al.*, 2000). The use of the optical trap to

dissect single myosin function showed that the functional consequence of the R403Q mutation is a result of reduced coordination between the ATPase cycles of myosins in myosin thick filaments.

Myosin II has a low duty ratio (fraction of the ATPase cycle time spent tightly bound to the actin filament; Marston and Taylor, 1980) with dwell times on the order of 10 ms at saturating ATP concentrations and a stroke size of ~ 10 nm. These small stroke sizes and short dwell times are likely resolvable with the noise and frequency response of the trap described here. To facilitate the separation of such short binding events and to distinguish them from the Brownian motion of the trapped bead, the technique of mean–variance analysis has been used (Guilford et al., 1997).

Unconventional myosins, such as myosin V and VI, by contrast, are high duty ratio motors with significantly larger dwell times (~ 100 ms) and stroke sizes (>20 nm). Whereas single dimeric molecules of myosin II are non-processive, dimeric forms of myosin V and VI are processive motors (Mehta et al., 1999; Rock et al., 2001). A processive motor takes multiple steps along an actin filament without detaching from it. Processivity requires the myosin molecule to be dimeric and have a high duty ratio, such that the leading head remains attached to the actin filament while the trailing head releases and finds its next binding site. Processive motors such as myosin V and VI take several steps along an actin filament in the trap. This feature combined with their long dwell times and large stroke sizes have enabled the use of the optical trap to dissect the workings of the myosin mechanoenzyme in great detail over the last decade (Spudich, 2001; Spudich and Sivaramakrishnan, 2009).

Unlike myosin II, which has two light chains bound to its lever arm (Rayment et al., 1993), myosin V has six (Kad et al., 2008). Purcell et al. (2002) used single-headed truncated versions of myosin V in the dual–beam optical trap to show that the larger stroke of myosin V (~ 25 nm) compared with myosin II (~ 10 nm) is a result of the lever arm that is six light chain-binding domains long. Using a dual–beam optical trap, Veigel et al. (2002) dissected the ~ 36 nm processive step of dimeric myosin V (Mehta et al., 1999) to reveal that it consists of a ~ 25 nm stroke of the lead head, followed by preferred binding of the free head 72 nm from its previous binding site (equivalent to a 36 nm movement of the center of mass of the dimer). The dual–beam optical trap provided adequate time resolution to discern that the 25 nm working stroke consists of two substeps of 20 and 5 nm, respectively. Using the kinetic parameters obtained from analysis of the optical trapping data, the authors suggested that the second 5 nm substep acts to increase processivity by coordinating the release of the rear and lead heads of the motor. This coordination, also referred to as "gating," leads to a hand-over-hand motion of myosin V and has since been observed directly using other single-molecule assays (Churchman et al., 2005; Dunn and Spudich, 2007; Sakamoto et al., 2008). Gating results from intramolecular strain that

changes the kinetics of the lead and trailing heads. This change in kinetics has been directly demonstrated by the application of forward and backward load on the trailing and leading head, respectively, using a dual–beam optical trap with directional load applied by oscillating either the platform (Purcell *et al.*, 2005) or the actin dumbbell (Veigel *et al.*, 2005). Similar studies in the presence of free phosphate in solution (Kad *et al.*, 2008) examined the interplay between phosphate release and load in the stepping cycle of myosin V. Taken together, optical trapping studies of myosin V have yielded significant insights into the chemomechanical coupling of this mechanoenzyme (Kad *et al.*, 2008).

Optical trapping of monomeric myosin VI constructs with varying lever arm lengths revealed a large $\sim 180°$ swing of their lever arm (Bryant *et al.*, 2007) compared to an only $\sim 70°$ swing of the lever arms of myosin II and V (Dominguez *et al.*, 1998). Crystal structures of myosin VI have supported this result from single–molecule optical trapping (Bryant *et al.*, 2007). Myosin VI has an unusual lever arm composed of two light chain-binding domains followed by a globular proximal tail and a relatively rigid single ER/K α–helical protein, which together contribute to a large stroke of ~ 30 nm by a myosin VI monomeric construct (Sivaramakrishnan *et al.*, 2008). The 180° powerstroke of myosin VI has been used to apply a defined mechanical force on ER/K α–helices of varying lengths (Sivaramakrishnan *et al.*, 2009). These optical trapping studies combined with small angle X-ray scattering and Monte Carlo simulations of the ER/K α–helix as a worm-like chain have enabled Sivaramakrishnan *et al.* (2009) to calculate its persistence length to ~ 15 nm. This study demonstrates the use of myosin to apply reproducible piconewton forces on protein molecules that are tethered to the end of its lever arm.

3. Optical Trap Instrumentation

3.1. Basic concept of an optical trap

Light has momentum and a force is generated when the momentum is changed. When light passes through an interface between two different media, reflection and refraction occur at the interface. As a simple example, consider a laser beam that is focused at the center of a spherical object that has a higher refractive index (n) than the surrounding aqueous medium. Reflection of light at the surface of the object generates a force (radiation force) on the object, in the direction of light propagation, with a magnitude proportional to the beam power. Refraction of light, on the other hand, produces a force (gradient force) that attracts the object to the focal point of the light beam, with a magnitude proportional to the gradient of beam power. The object is ''trapped'' at a point where the vector sum of the

gradient and radiation forces is zero (Ashkin, 1992). This point is referred to as the center of the trap and is located near the focal point of a high numerical aperture (NA) microscope objective lens (NA > 1.2, and most often 1.4). Good optical trapping is often accomplished by slightly over-filling the back aperture of a high NA objective lens with a Gaussian beam, to obtain a diffraction limited spot.

For biological applications, where the optical trap is used to apply a force on a single protein/DNA molecule, the trapped object is usually a polysty-rene ($n = 1.57$) microsphere ranging in size from several hundred nan-ometers to a few microns. The force experienced by the trapped object increases linearly with distance from the trap center. The strength of the trap is expressed in terms of the ''trap stiffness'' and varies for most applica-tions from 0.005 to 1 pN/nm. The force experienced by the trapped object is, therefore, the product of the trap stiffness and distance from the trap
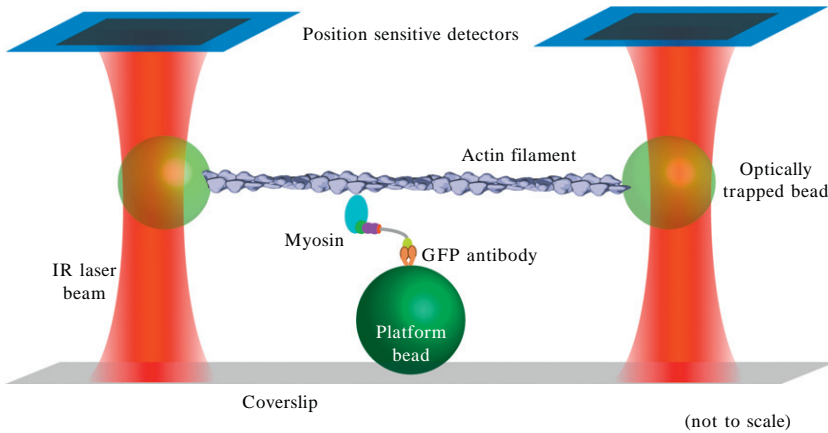
Figure 14.1 Dual–beam, three-bead optical trapping assay for the study of myosins. Schematic of a dual–beam laser optical trap for measuring the lever arm stroke, force generation, and kinetics of single myosin molecules. Two neutravidin-coated polystyrene beads ($\sim 1\ \mu m$, light gray) are optically trapped by focused infrared (IR) laser beams. A single biotinylated actin filament (9 nm diameter) is attached at its ends to the two optically trapped beads. The actin filament is stretched taut ($\sim 10\ \mu m$ long) by moving the two trapped beads away from each other by independently controlling each laser beam. Illustrated here is a myosin VI monomer with a C-terminal GFP-tag attached to a $\sim 1.5\ \mu m$ polystyrene platform bead (dark gray) coated with anti-GFP antibody. The position of each of the trapped beads is determined accurately by two position-sensitive detectors (PSD) located in the optical path above the trapped beads. Each PSD is optically conjugated with the back–focal plane of the condenser (not shown). *Note*: For purposes of clarity, the components in the figure are shown at different length scales.

bright-field illumination to image beads, and fluorescence illumination to image actin filament (Figs. 14.2 and 14.3). In this section, we provide an overview of the dual–beam trap setup. Details of the setup are described later (see alignment, Section 3.4). Further description of the setup can also be found in the legends of Figs. 14.2–14.4.

The trapping laser and beam steering optics enable us to trap the two beads and independently control their position, which is essential to make a tight actin dumbbell (Fig. 14.2, panel 1). A pair of polarizing beam splitters (PBS2, PBS3) separate and recombine the p– and s–polarized components of the trapping beam. Piezo-driven mirror mounts (PM1, PM2) are used for independent coarse positioning of the dual trapping beams to enable the formation of the actin dumbbell. We use a pair of acousto-optic deflectors (AOD) for fast ($\sim 1\ \mu s$) and precise (~ 1 nm) control of trap position during the feedback control. This fast and precise feedback control of the trap beam is essential for the study of processive motors such as myosin V. In order to make a stable actin dumbbell, the distance between the two trapped beads must be kept constant. This is achieved by minimizing the path length

Dual-beam optical trap setup

(not to scale)

1 Trapping laser (1064 nm) — M4, M3, X, AOD, Y, Fiber, Out, B, D, s, p, PBS1, ISO1, M1, L1, Iris1, HP1, M2, L2, M5, HP2, PBS2, p, s, PM1, PM2, S1, S2, PBS3, L3, Iris2, M6

3b Detection laser (850 nm) — ND3, L8, L9, PM3, PBS5, p, s, HP3, M8, PBS6, L10, PM4, Iris4, DM5, L4

4a LED 740 nm — L6, ND1, DM2

3a PSD2, L13, F1, s, p, L5, PSD1, PBS4

2 CON, Piezo stage, x-y stage, OBJ, DM1, M7

4b CCD 1, L7, DM4, F2, L12, CCD 2, DM3, L11, ND2, M9

5 Fluorescence laser (532 nm), M10

1. Trapping laser and beam steering
2. Microscope
3. Detection laser and bead position detector
4. Bright field illumination
5. Fluorescence illumination

▪▪▪▪ Optically conjugated planes
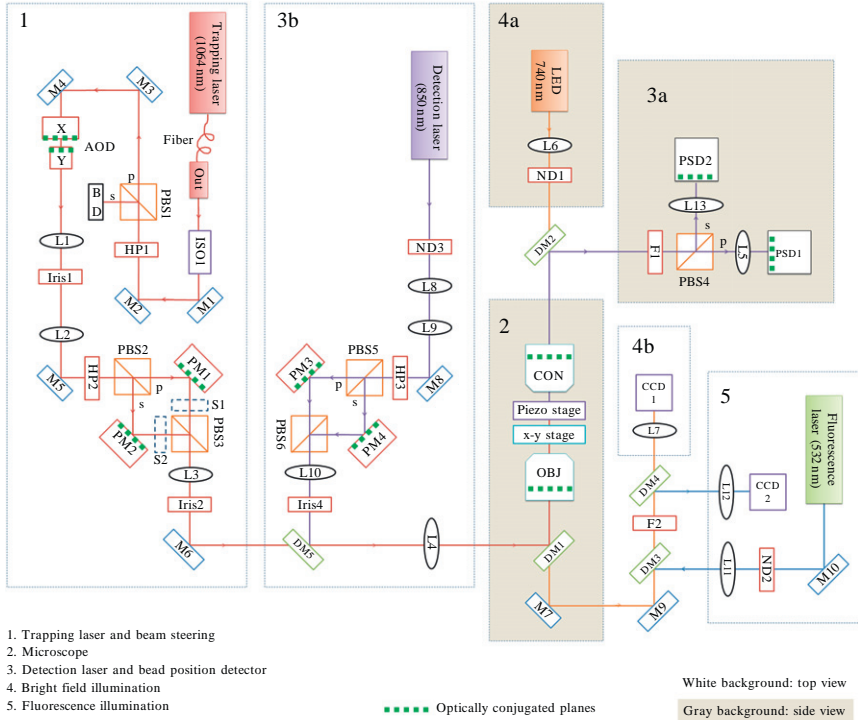
White background: top view
Gray background: side view

Figure 14.2 Design of a dual-beam optical trap for the three-bead assay. The setup consists of five main parts: (1) trapping laser and beam steering, (2) microscope, (3) detection laser and bead position detector, (4) bright-field illumination, and (5) fluorescence illumination. Note that the white background is the top view while the gray background is the side view. Specific information of each component is found in Table 14.1. (1) Trapping laser and beam steering (panel 1): a collimated 1.6 mm trapping laser beam from a 1064 nm ytterbium-doped fiber laser passes through an isolator (ISO1), which protects the fiber laser from back reflections from any downstream components. Mirrors 1 and 2 (M1, M2) adjust the beam path such that it is parallel to the surface of the optical table. A half-wave plate (HP1) and polarizing beam splitter (PBS1) control the final power of the trapping beam, which is p-polarized. The s-polarized component is dissipated into a beam dump (BD). Alternately, the s-polarized beam can be used for single-beam feedback control (described in Section A.2). There are two different beam steering controls: fast and precise beam steering uses the acousto-optic deflectors (AODs), and slow and coarse beam steering uses the piezo-driven mirror mounts (PMs). The AODs are followed by a telescope with two lenses L1 and L2, which allow optical conjugation of the AODs and PM1/PM2. The PMs are followed by a telescope with two lenses L3 and L4 that optically conjugate the PMs with the back aperture of the objective lens (OBJ). Therefore, both AODs and PMs are conjugated with the OBJ back aperture (gray dotted lines). This allows us to use the AODs for fast and precise control of the optical trap, especially during feedback control of trap position for processive dimeric motors, such as myosin V. PMs, on the other

between PBS2 and PBS3 since it reduces the differential effects of air fluctuation and mechanical vibration on the separated beams. The AODs operate on the combined beam, contrary to previous designs (Rice *et al.*, 2003). In this configuration (Fig. 14.2, panel 1), the AODs cannot be used to steer two trapped beams independently. This feature does not affect studies on myosin function, which we use as an example in this chapter. For studies that require fast feedback control of just one bead, please refer to a subtle modification in this design discussed in Section A.2.

hand, allow the relatively slow and coarse positioning of beads, which is essential for making a taut actin dumbbell. Two sets of telescopic lenses (L1–L4) expand the beam diameter sixfold (from 1.6 to 9.6 mm), so the final beam slightly (10%) overfills the back aperture of OBJ ($D = 9.6$ mm). The second half-wave plate (HP2) followed by two beam-splitters (PBS2/PBS3) create two independent beam paths (s- and p-polarized) that can be steered independently using PM1 and PM2. Two shutters (S1, S2) can be placed between PBS2 and PBS3, such that the two trapping beams can be independently turned on and off. For the distance between each component, see Figs. 14.3 and 14.4. (2) Microscope (panel 2): the steered trapping beam is reflected by the first dichroic mirror (DM1) and passes through the OBJ (NA = 1.45) which focuses it in the sample chamber. The condenser (CON) (NA = 1.35) collects the transmitted beams, which forms interference patterns at the back–focal plane (BFP, gray dotted line) of the CON. The interference patterns are produced from the combination of unscattered incident beams and forward scattered beams from the trapped beads. (3) Detection laser and bead position detector (panel 3): (a) bead position detector— following the CON, the trapping beams are reflected on a dichroic mirror (DM2) followed by two lenses L5/L13 that image the BFP interference patterns at two position-sensitive detectors (PSD1/PSD2) for dual traps. A band-pass filter (F1) is used to attenuate 1064 nm trapping beams. (b) Detection laser—the 850 nm laser beams are used for the detection of the beads. While the 1064 nm trapping laser beams can be used directly to detect trap position, in the three-bead assay discussed here, additional 850 nm laser beams are used for improved accuracy (described in the text). The function of components in the 850 nm laser beam paths is similar to that of the trapping laser. A neutral density filter (ND3) provides optimum power for detection. PM3 and PM4 independently control the position of the detection laser beams relative to the trapped beads. A dichroic mirror (DM5) allows the detection beams to be coupled to the trapping beams. (4) Bright-field illumination (panel 4): we visualize the beads in the sample plane using bright-field illumination with a 740 nm LED light source. A lens (L6) collects a diverging beam from the LED and sends it through a dichroic mirror (DM2) to the CON. The bright-field beam emerges from the OBJ, passes through DM1, and is focused on a charge-coupled display (CCD1) by a tube lens (L7). (5) Fluorescence illumination (panel 5): a 532 nm laser is used to obtain a fluorescence image of the actin filament labeled with fluorescent phalloidin (tetramethylrhodamine (TMR)-phalloidin dye). The fluorescence image is necessary to make a single actin dumbbell between the two trapped beads. DM3 reflects the excitation beam (532 nm), and DM4 reflects the fluorescence (580 nm) of the TMR dye. A tube lens (L12) makes a fluorescent image of the sample plane on CCD2. The focal length of the lenses are L1 = 100 mm, L2 = 200 mm, L3 = 100 mm, L4 = 300 mm, L5 = 75 mm, L7 = 200 mm, L8 = 100 mm, L9 = 200 mm, L10 = 100 mm, L11 = 250 mm, L12 = 200 mm, and L13 = 75 mm.
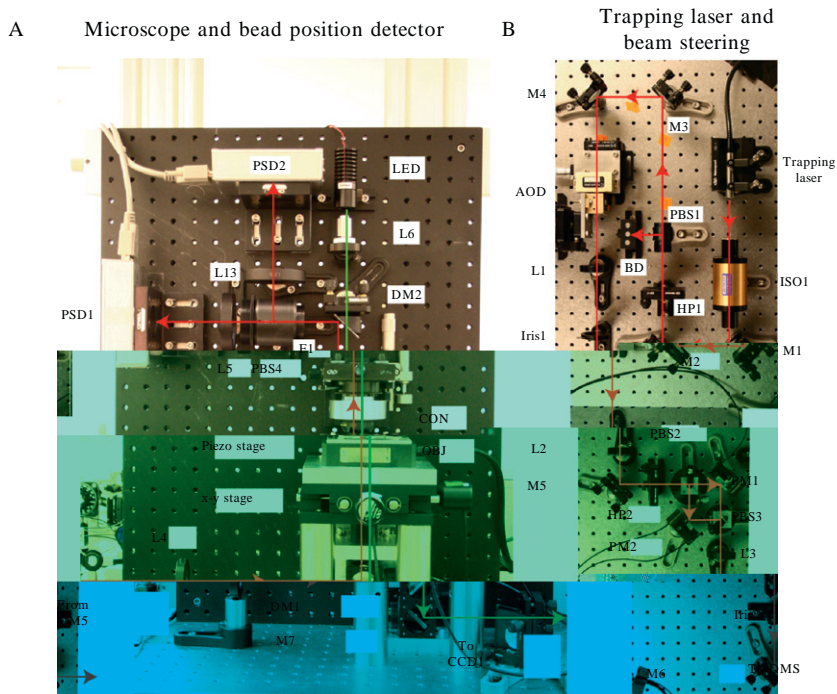
Figure 14.3 Photographs of the actual dual-beam optical trap setup. The primary components of the setup in Fig. 14.2 (microscope, bead position detector, and trapping laser and beam steering) are shown here. (A) Photograph of the microscope and the bead position detector setup. (Green arrow) Beam path from the bright-field light source (LED) to the detector (CCD1)—a diverging beam from the LED light source (740 nm) is collected by a $10\times$ objective lens (L6). The distance between holes in the bread-board is 1 in. Condenser (CON) is mounted on a gimbal optics mount and a z-translation stage. The distance between LED and the front aperture of CON is ~ 11 in. CON collects and focuses the beam into the sample channel which is mounted on the top of the piezo stage during experiments. Objective lens (OBJ) (obscured from view by the piezo stage) collects the beam from the sample plane, and sends it downwards. The mirror turret with dichroic mirror DM1 and reflective mirror M7 is mounted on the optical table, with DM1 and M7, respectively, 3 and 1.5 in. above the table surface. The beam reflected by M7 is collected by a tube lens (L7, $f = 200$ mm, not shown in figure) which images the sample plane on CCD1. (Red arrow) Trapping/ detection beam paths from DM5 to the detectors (PSD1, 2)—trapping/detection beams pass through a lens L4 and are reflected on a dichroic mirror DM1. The OBJ focuses the beams in the sample channel and CON collects the transmitted beams. The beams are reflected on a dichroic mirror DM2, pass through F1, PBS4, L5/L13, and finally arrive on the sensors (10 mm^2) of PSD1, 2. We adjust the height of CON such that the transmitted beams ($D \sim 20$ mm at the CON) are collimated. The distance between the BFP of CON and L5 is ~ 230 mm, and the distance between L5/L13 and PSD1/PSD2 is ~ 110 mm. The interference patterns at the BFP of CON are demagnified by a factor of ~ 2 ($M = \frac{110\,\text{mm}}{230\,\text{mm}} \sim \frac{1}{2}$). A filter F1 is mounted on a flipping mount such that it selectively transmits the 850 nm detection laser beams but blocks the 1064 nm beams when it is

The microscope body is set up to accommodate a slide–coverslip sand-wich with sample channel (Fig. 14.2, panel 2). The objective lens (OBJ) brings the trapping beam to a focal point in the sample plane. This focused trapping beam generates a restoring force that holds a trapped bead at the center of the trapping beam. The piezo stage (P-731.20, Physik Instru-mente) and motorized x–y stage are used for fine and coarse control, respectively, of the position of the platform bead in the sample channel (Fig. 14.2, panel 2). A piezo-based actuator is used to change the distance of the sample plane from the coverslip surface.

For detecting the bead position, we use the back focal plane detection method (Gittes and Schmidt, 1998a; Pralle *et al.*, 1999). Two position-sensitive detectors (PSD1 and PSD2; Fig. 14.2, panel 3a) are used for the detection of each of the two beads. Back focal plane detection could be done using the trapping beam as the detection laser (Gittes and Schmidt, 1998b). However, this is not appropriate for the three-bead assay shown in Fig. 14.1. The trapping beam is not centered on the trapped bead, and this can result in a nonlinear relationship between the back focal detection signal and the bead displacement. To avoid this potential complication, we use a separate detection laser that is centered on the bead (Fig. 14.2, panel 3b) (Neuman and Block, 2004). The positions of the dual detection beams are controlled independently by PM3 and PM4 (see Section 3.2.6). We use PBS5 and PBS6 in conjunction with PM3 and PM4 for independent position control of the detection laser beams (Fig. 14.2, panel 3b).

Imaging the beads and the actin filament is essential for trapping the beads and creating the actin dumbbell. An LED (740 nm) is used to

flip-in position. When we use trapping beams for the detection, the F1 is switched to the flip-out position. PSDs are mounted on custom boxes and L-brackets for the stability of the detectors, and the input and output connections of the PSD with power supplies and NI-DAQ are accomplished though the cable mounted on the box. (B) Photograph of the trapping and the beam steering parts setup—the fiber output of the trapping laser (the body is separately mounted off the table) is stably mounted on a V-block mount followed by an ISO1 at 5 in. from the fiber. Mirrors M1 and M2 (4 in. separated) redirect the beams to the pair of HP1 and PBS1 which allows controlling of the trap beam power. The initial beam size is 1.6 mm. Mirrors M3 and M4 redirect the beams to the fast beam steering components (AOD, L1, L2) followed by the slow beam steering components (PM1, L3, L4 (not seen)). Here, the position of AOD, L1, L2, and PM1/PM2 satisfies the *4f arrangement* condition, whose separations are L1, L1 + L2, and L2, respectively. The second pair of HP2, PBS2, and PBS3 separates and recombines the p- and s-polarized beams for independent control of the dual beams. Rotation of the HP2 determines the relative stiffness of the dual beams, and usually we make the trap stiffness of the two beams the same to maximize the stability of the actin dumbbell. The difference of each beam path between PBS2 and PBS3 is 4 in. in our setup, such that noise sources (mechanical vibration and air fluctuation) arising out of them affect the dual beam by the same amount. Note that the distance between the threaded mounting holes on the optical table is 1 in.
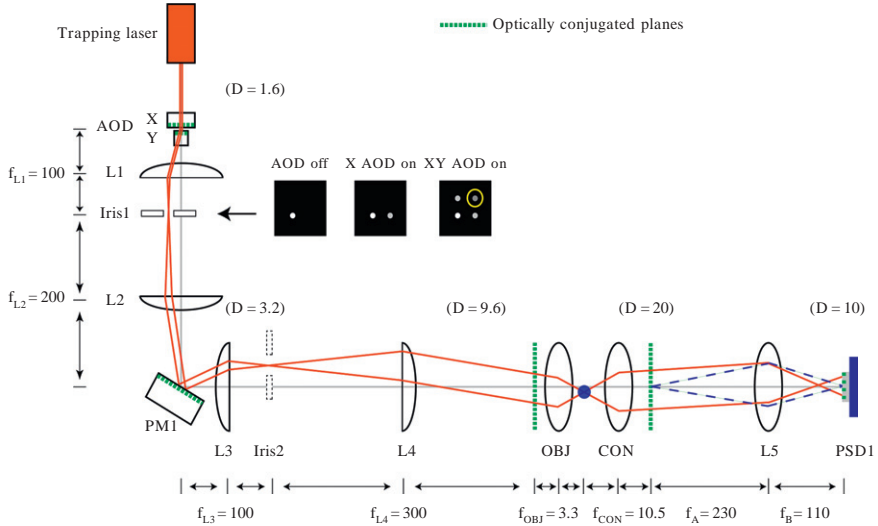
Figure 14.4 Beam path in a single-beam optical trap—the primary components of the dual-trap setup in Fig. 14.2 are shown here for a single-beam trap, with detailed information on the distance between each component and the beam layout. The initial size of the trapping beam is ~ 1.6 mm. The combination of AOD, L1 ($f_{L1} = 100$ mm), L2 ($f_{L2} = 200$ mm), and PM1 forms a *4f arrangement* for fast and precise beam steering. Multiple deflected beams (four strong beams) are produced by the AOD, transmitted through L1, and focused in the focal plane of L1. Iris1 transmits only the first-order diffracted beam from the two AODs, as seen in the right panel labeled "XY AOD on." The beam between L2 and L3 is collimated with diameter ~ 3.2 mm. Another combination of PM1, L3 ($f_{L3} = 100$ mm), L4 (($f_{L4} = 300$ mm), and back aperture of OBJ forms the second *4f arrangement* for the slow and coarse beam steering. The beam steering of PM1 results in the steering of the beam entrance into the back aperture of OBJ such that the trapped bead translates linearly in the sample plane. The beam is collimated with size ~ 9.6 mm, which slightly (10%) overfills the back aperture of OBJ. AODs, PM1, and the back aperture of OBJ are all optically conjugated (dotted gray lines), assuring that the deflected beam is always delivered into the back aperture of OBJ without beam clipping during the beam steering. The trapping beam passing through the trapped bead is collected and collimated by CON (beam size ~ 20 mm). L5 (($f_{L5} = 75$ mm) images the back-focal plane (BFP) of CON as drawn in the blue dashed line. Note that the optically conjugated planes are all expressed as dotted green lines shown at the AODs, PM1, BFP of OBJ and CON, and PSD1. The trapping beam is coupled with the detection beam between L4 and OBJ such that the detection beam path is following the same beam path in the detection part.

illuminate the sample plane (Fig. 14.2, panel 4a). A bright-field image of the sample plane is captured by CCD1 (Fig. 14.2, panel 4b). A fluorescence laser (532 nm) is used to excite the fluorescent phalloidin (tetramethylrhodamine (TMR)-phalloidin, Sigma-Aldrich) bound to the actin with the emission being imaged on CCD2 (Fig. 14.2, panel 5). Alternatively, we are exploring the use of another dye (CF 405 phalloidin, Biotium) with a

405 nm laser excitation to leave the green and red portions of the visible spectrum open for future simultaneous optical trapping/fluorescence imaging experiments (Hohng *et al.*, 2007; Ishijima *et al.*, 1998; Lang *et al.*, 2004; van Dijk *et al.*, 2004).

The following sections describe the most important components of the setup in detail. Specific information on all components is found in Table 14.1.

3.2.1. Trapping laser

A typical laser for a dual–beam optical trap is a single mode (Gaussian TEM_{00}), continuous wave (CW) laser of single wavelength ranging from 800 to 1100 nm with a power output ranging from 1 to 5 W (Bustamante *et al.*, 2007; Neuman and Block, 2004). Important features of the laser for a stable trap are its maximum power, power stability, pointing stability, and beam profile. For a detailed description of criteria for selection of a suitable trapping laser, we refer the reader to Neuman and Block (2004) and Bustamante *et al.* (2007). Our trapping laser is a 5 W, 1064 nm, fiber laser from IPG (YLR-5-1064-LP). It is a diode-pumped, TEM_{00} ($M^2 < 1.1$), linearly polarized CW ytterbium laser with a quoted power instability of $<3\%$ over 4 h ($<2\%$ in the 1 kHz to 20 MHz range) and good pointing stability (~ 1 μrad). We chose a fiber laser, as it provides good pointing and power stability. Fiber coupling allows us to position the laser body and power supply away from the optical table, which reduces vibrations and improves trapping stability. This fiber laser ($\sim\$15,000$) is less expensive than conventional trapping lasers (diode-pumped solid-state lasers $\sim\$30,000$).

3.2.2. Objective (OBJ)

Important features of an OBJ for a good trap are its NA and transmittance. High NA (> 1.2, and often > 1.4) generates a power gradient sufficient to overcome the radiation force, which results in a stable optical trap. Either an oil or water immersion OBJ can be used for an optical trap. An oil immersion OBJ typically has a higher NA than a water immersion OBJ. One potential problem of using an oil immersion OBJ is the spherical aberration that arises when the beam is focused deep in the solution (more than a few micormeters) due to the index mismatch between the aqueous medium ($n \sim 1.32$) and the immersion oil ($n = 1.512$). The three–bead assay requires focusing the trapping beam close to the coverslip surface (~ 1.5 μm distance) where the spherical aberration is not significant, and an oil immersion OBJ is appropriate for this purpose. Our current OBJ is a CFI Plan Apo oil immersion TIRF objective lens (MRD01602, Nikon) with high NA (1.45) and transmittance (60% at 1064 nm).

Table 14.1 Primary components of the dual-beam optical trap setup

	Company	Model number	Description
Optical table	Technical Manufacturing Corporation	784–35631–01	Top thickness—18 in. (300 mm), top length—8 ft (2.4 m), minimum resonant frequency 200 Hz
Trapping laser	IPG	YLR–10-1064–LP	Diode-pumped CW, ytterbium-doped fiber laser, max power 5 W, wavelength 1064 nm, beam diameter 1.6 mm, TEM00 mode, M2 < 1.1, linearly polarized, power stability <3% (over 4 h) and <2% (1 kH to 20 MHz range), and pointing stability ~1 μrad, fiber length 2 m
Detection laser	World Star Tech	TECIRL–30GC–850	Diode laser, CW, power 30 mW, wavelength 850 nm, beam diameter 1.6 mm, circular, linearly polarized, power stability <0.5%, temperature control, pointing stability <25 μrad (in spec), pointing stability ~1 μrad (measured over 300 s)
Fluorescence laser	Coherent	Compass 215M-20	DPSS laser, CW, power 20 mW, wavelength 532 nm, beam diameter 0.32 mm, TEM00, M2 < 1.1, pointing stability <6 μrad/C, noise (10 Hz to 1 GHz) <0.5% (rms)
Fluorescence laser	World Star Tech	TECBL-10G-405	Diode laser, CW, power 10 mW, wavelength 405 nm, beam diameter 1.6 mm, circular, linearly polarized, temperature control
LED	Mightex	SLS-0111-A	740 nm, 120 mW luminous flux, lens A (narrow beam, 19 mm aperture, half angle 5°, efficiency 85%)
Objective lens	Nikon	MRD01602	TIRF, CFI Plan Apo, magnification 60× VC, NA 1.45, oil immersion, transmittance 60% for 1064 nm

Table 14.1 (*continued*)

	Company	Model number	Description
Condenser	Nikon	T-C HNA-oil lens	MEL41410, $f = 10.5$ mm, NA 1.35
Isolator	Thorlabs	IO-5-1064-VHP	Free space isolator, 1064 nm, 4.8 mm aperture, 100 W (max)
Z-translation stage for objective lens	Newport	462-X-SD	462 ULTRAlign^{TM} precision integrated crossed-roller bearing linear stage, 1.0 in. X travel, slide drive
Z translation actuator for objective lens	Newport	PZA12	NanoPZ ultra-high resolution actuator, 12.5 mm travel
	Newport	PZC200	Hand-held controller for PZA12
X–Y translation actuator for sample stage	Newport	406	High-performance large platform two-axis linear stage, aperture platform, 1/4–20 tapped holes
X–Y translation stage for sample stage	Newport	NSA12	11 mm travel motorized miniature linear actuator
	Newport	NSC200	NewStep hand-held motion controller for NSA12
Tube for mounting of OBJ	Thorlabs	SM1L20	SM1 lens tube, 2 in. long, one retaining ring included
Piezo stage	Physik Instrumente	P-731.20	High-resolution XY-positioning stages, range: 100 μm, resonant frequency: 400 Hz, resolution: 1 nm
Breadboard	Thorlabs	MB1824	Aluminum breadboard, 18 in. $\times$ 24 in. $\times$ 1/2 in., ¼-20 threaded
Rail	Thorlabs	XT95-750	95 mm construction rail, $L = 750$ mm
Rail base	Thorlabs	XT95P3	Optical table base plate
Microscope body post	Thorlabs	P6	Mounting post, length $= 6$ in.

Mounting cube for mirror turret (DM1, M7)	Linos	G061-081-000	Cube 40 mm × 40 mm, $D = 30$ mm
	Linos	G061-207-000	Rods 20 mm
	Linos	G065-087-000	Beam steering mirror holder 30
	Linos	G061-011-000	Set of screws M2.3×3 (qty. 150)
	Linos	G061-012-000	Set of threaded pins M2.3×6 (qty. 150)
DM1	Chroma	t800dcspxr	Shortpass, T: 405–740 nm, R: 850, 1064 nm
DM2	Chroma	780dcspxr	Shortpass, T: 740 nm, R: 850, 1064 nm
DM3	Chroma	r532rdc-xt	Longpass, T: 540–1064 nm, R: 532 nm
DM4	Chroma	700dcxr	Longpass, T: 740–1064 nm, R: 460, 580 nm
DM5	Chroma	940dcxr	Longpass, T: 1064 nm, R: 850 nm
Dichroic mirror mount	Newfoucs	9920	45° mirror holder
F1	Thorlabs	FB850-40	Bandpass filter, CWL = 850 nm, FWHM = 40 nm
F2	Thorlabs	FES0800	Shortpass filter, cut-off wavelength: 800 nm
HP1, HP2	Newport	10RP02-34	Zero-order quartz wave plate, 25.4 mm dia, 1064 nm, $\lambda/2$ retardation, 2 MW/cm^2 CW
HP3	Newport	05RP02-30	Zero-order quartz wave plate, 12.7 mm dia, 850 nm, $\lambda/2$ retardation
PBS1	Newport	05BC16PC.9	Laser line polarizing cube beamsplitter, 12.7, 1064 nm
PBS2, 3	Newport	10BC16PC.9	Laser line polarizing cube beamsplitter, 25.4, 1064 nm
PBS4	Newport	10FC16PB.7	Broadband polarizing cube beamsplitter, 25.4 mm, 850–1300 nm, 2 kW/cm^2 CW
PBS5, 6	Newport	05FC16PB.5	Broadband polarizing cube beamsplitter, 12.7 mm, 620–1000 nm
M1–M6, mirrors for PM1, 2	Newport	10D20DM.10	Laser line dielectric mirror, Pyrex, 25.4 dia, 6.0 mm, $\lambda/10$, 1030–1090 nm
M8, mirror for PM3, 4	Thorlabs	BB1-E03	Ø1 in. broadband dielectric mirrors, 750–1100 nm

(*continued*)

Table 14.1 (*continued*)

	Company	Model number	Description
M7	Linos	G340–523–000	Silver elliptical plane mirrors, laser quality, 22.4 mm × 31.5 mm × 3.5 mm
Mirror mount	Thorlabs	KM100	Kinematic mirror mount for 1 in. optics
L1, L3	Newport	KPX094AR.33	BK 7 plano-convex lens, 25.4 dia, 100 EFL, 1064 nm
L2	Newport	KPX106AR.33	BK 7 plano-convex lens, 25.4 dia, 200 EFL, 1064 nm
L4	Thorlabs	LA1256–B	N–BK7 plano-convex lens, Ø2 in., $f = 300.0$ mm, ARC: 650–1050 nm
L5, L13	Thorlabs	LB1309–B	N–BK7 bi-convex lens, Ø2 in., $f = 75$ mm, ARC: 650–1050 nm
L6			10× objective lens
L7, L9	Thorlabs	LA1708–B	N–BK7 plano-convex lens, Ø1 in., $f = 200.0$ mm, ARC: 650–1050 nm
L8, L10	Thorlabs	LA1509–B	N–BK7 plano-convex lens, Ø1 in., $f = 100.0$ mm, ARC: 650–1050 nm
L11	Thorlabs	LA1461–A	N–BK7 plano-convex lens, Ø1 in., $f = 250.0$ mm, ARC: 350–650 nm
L12	Thorlabs	LA1708–A	N–BK7 plano-convex lens, Ø1 in., $f = 200.0$ mm, ARC: 350–650 nm
Lens mount	Thorlabs	LMR1	Lens mount for Ø1 in. optics, one retaining ring included
Mount for trap beam fiber	Newport	VB-1	V–Block, 3 in. (76.2 mm) length

For most of the mirrors mount, we use 1 in. diameter post RS2P (Thorlabs) with clamping fork CF125 (Thorlabs)

For most of the lens mount, we use 1 in. diameter post exc2867nt RS. (Thorlabs) withRB2r

AOD	IntraAction	DTD-274HA6	2-axis acousto–optic deflection system
AOD RF source	IntraAction	DVE-120	Dual RF frequency source (PCI)
AOD RF amplifier	IntraAction	DPA-502D	Dual RF power amplifier
PM1–4 mount	Newport	AG-M100N	Agilis mount, 1.0 in. (25.4 mm), range ± 2 deg, sensitivity 1 μrad, max speed 0.75 deg/s
PM controller	Newport	AG-UC8	Agilis compact 8-axes controller, USB interface
PSD1, 2	Pacific Silicon Sensor	DL100-7PCBA3	X, Y duolateral position sensing photodiode with sum difference circuitry. Includes connector and variable bias option. Active area 10 mm $\times$ 10 mm
CCD1	Watec	WAT 902H2 Supreme	Watec WAT 902H2 Supreme B/W 1/2 in. camera low lux
CCD2	Hamamatsu	C2400-08	Real-time fluorescence imaging, 400–850 nm spectral response
NI-DAQ	NI	779068-01	NI PCI-6229
Cable for NI-DAQ	NI	192061-01	SHC68-68-EPM Cable (1 m)
Connector block for NI-DAQ	NI	777960-01	BNC-2120—shielded
Labview	NI	LabVIEW 8.6	
Matlab	Mathworks	Matlab R2009a	
TMR phalloidin	Sigma–Aldrich	P1951	Ex peak: 552 nm, Em peak: 580 nm, phalloidin–tetramethylrhodamine B isothiocyanate conjugated with phalloidin
CF405 dye	Biotium	00034	Ex peak: 405 nm, Em peak: 460 nm, conjugated with phalloidin
Immersion oil	Nikon	MXA22024	50cc NonFluor immersion oil
IR sensor	Newport	F-IRC2-S	IR sensor card, 800–1700 nm, 1 in. $\times$ 1.5 in. sensor

3.2.3. Microscope body

The microscope body can either be purchased from commercial manufacturers or custom-made (Fig. 14.3A). The main advantage of using a custom-made body is the enormous flexibility in the design of the objective–condenser assembly, with easy positioning of the PSD and detection units. Furthermore, customized microscope bodies are more cost-effective than commercial bodies. An important measure of a good microscope body is the stable positioning of its components. In the three-bead assay, we quantify the interaction between a myosin molecule immobilized to the coverslip surface and an actin filament suspended between two independently trapped beads. Fluctuations in the relative position of components in the microscope body add to the noise in the bead position measurements. Thus, for an accurate measurement of actin interactions with myosins, which displace the trapped beads by tens of nanometers over millisecond time scales, fluctuations in the microscope body should be an order of magnitude smaller than the myosin-driven actin movements. We use a breadboard mounted on a rail (MB1824, XT95-750, Thorlabs) for the vertical mounting of the microscope, PSD, and LED (Fig. 14.3A). This gives us flexibility in the optical path layout as well as excellent stability. The adaptors that interconnect each component of the microscopy body were machined in house.

3.2.4. Beam steering for slow and coarse positioning

The spatial position of each of the trapped beads in the sample plane needs to be controlled independently in the three-bead assay. This is essential for trapping the two beads and steering them to create a taut actin filament between the beads. The spatial position of the trapped beads can be controlled independently by piezo-driven mirrors PM1 and PM2 (AG-M100N, Newport) (Fig. 14.2, panel 1). Alternate configurations have been used for coarse steering (Rice *et al.*, 2003). The advantages of PMs in the current configuration are their compactness, high sensitivity, improved stability, and low cost ($\sim$\$1000 per PM with the controller). The compactness of PMs minimizes the distance over which the two trapped beams pass through separate optical paths. In our current design, this distance reduces to 4 in. Minimizing this distance reduces the contribution of environmental noise arising from mechanical vibration or air flow fluctuations (Bustamante *et al.*, 2007; Moffitt *et al.*, 2006) and improves the stability of the actin dumbbell in the three-bead assay by maintaining the distance between the two traps. Our design provides a $\sim$20 μm range of coarse bead movement and a $\sim$10 μm/s maximum speed in the sample plane. The coarse beam steering of PMs is easily accomplished with either a controller or a custom Labview program (Labview 8.6, National Instruments).

3.2.5. Beam steering for fast and precise feedback control

Fast feedback control of the trapping beam is necessary for either a force clamp or a position clamp of the trapped bead. A force clamp is achieved by maintaining the relative distance between the trapping beam and the trapped bead position. Force clamping has proved to be a very powerful tool in the studies of processive motors, such as a myosin V, to obtain accurate step size and ATPase kinetics in the presence of compliant elements (Rief *et al.*, 2000; Veigel *et al.*, 2002; Visscher *et al.*, 1999). A position clamp is performed by maintaining the bead position as constant as possible (Finer *et al.*, 1994; Simmons *et al.*, 1996). Position clamping is achieved by changing the trap force to prevent bead movement. This technique has been used to measure the maximum force that a single myosin molecule can produce (Finer *et al.*, 1994). Both clamping techniques require fast update of the trap position over submillisecond timescales along with precise positioning over nanometer spatial scales. For detailed information regarding feedback control, see Visscher and Block (1998) and Spudich *et al.* (2007).

In our design, fast feedback control of the trap is achieved using an AOD. The setup described here is for our AOD model (DTD-274HA6, IntraAction). A PCI board for the dual RF frequency source (DVE-120, IntraAction) generates an RF signal (12 bits amplitude dynamic range, frequency access time ~ 1 μs). The signal is amplified through a dual RF power amplifier (DPA-502D, IntraAction). The full deflection range of our model is 26.9 mrad (16 MHz), which corresponds to ~ 15 μm displacement in the sample plane. With an AOD, only the first–order deflected beam is used, which results in a significant loss of beam power (at least 50%). Use of a high–power laser (5 W) compensates for this lost power in our design. Feedback control of the AOD is achieved with a custom Labview program.

3.2.6. Detection of bead position

Back focal plane detection is one of the most common methods to measure the position of the trapped beads (Gittes and Schmidt, 1998a; Pralle *et al.*, 1999; Visscher *et al.*, 1996) (Figs. 14.4 and 14.5C). At the back focal plane of the condenser, there is interference between the incident trapping beam and the forward scattered beam by the trapped bead. The center of mass of the interference pattern translates linearly with the relative position between the trapping beam and the trapped bead. A PSD or a quadrant photodiode (QPD) can measure the centroid of the interference pattern and thereby tracks the center of the trapped bead. We use a PSD (DL100-7PCBA3, Pacific Silicon Sensor) due to its low noise, linear response on the entire sensor (10 mm^2 area), and ready-to-use preamplifier circuit (Bustamante *et al.*, 2007; Huisstede *et al.*, 2006; Neuman and Block, 2004). Output of the PSD is an $x-y$ voltage signals for the x and y centroids of the beam, as well as the sum signals of them. The bandwidth of this detector, which is an upper
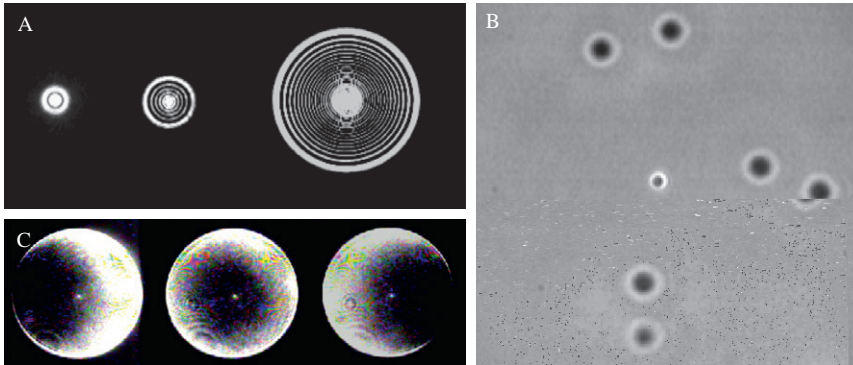
Figure 14.5 (A) Airy ring of the transmitted beam—an Airy disk of one of the transmitted trapping beams through the OBJ and CON can be visualized using a CCD camera, which can be temporarily positioned between CON and DM2 in Fig. 14.2. When the CON is positioned where the diffraction limited spot formed by the OBJ is imaged on the CCD, we see the smallest beam size (left panel). As the height of the CON moves away from the optimal position, the number of rings and the diameter of the diffraction pattern gradually increase from the left to the right as seen here. This is an indicator that shows the quality of the trapping beam. If any noticeable aberrations are shown in the pattern, the trapping beam is not able to make a symmetric diffraction limited spot in the sample plane. A symmetric diffraction pattern is essential for good trapping. (B) Bright-field image of the sample plane imaged on the CCD—the sample consists of 1.5 μm size polystyrene platform beads adsorbed to the coverslip surface, and a 1 μm size polystyrene trapped bead (center). The platform beads appear out of focus as the sample plane is several μm into solution, whereas the trapped bead is in focus. This is a representative image of the sample plane during the optical trapping experiments described in the text. In the dual-beam trap, the two trapped beads of an actin dumbbell are in focus, instead of the one trapped bead seen here. (C) Back-focal interference pattern imaged by a CCD—back-focal interference pattern of a bead can be visualized using a CCD which can be temporarily mounted in place of the PSD. As an example, we positioned a trapping beam near the center of a platform bead adsorbed on the surface. Lens L5 in Fig. 14.2 images the back-focal plane of the CON such that the destructive interference pattern is seen at the center of the beam (center panel). As the beam is steered by AOD or PM1, we see the shift in interference pattern as shown in the left and right panels. The PSD enables us to quantify the amount of the shift of the centroid of the bright portion of the interference pattern. The centroid displacement can be calibrated to the real displacement of the bead relative to the center of the trapping beam.

bound on the time resolution of the PSD, is 257 kHz, much faster than our current data sampling rate of the signal (10 kHz). Since the output of the PSD is merely a voltage signal that is affected by parameters such as power of the beam and shape and size of the bead, the PSD must be calibrated to convert the PSD voltage to nanometer distance change in position of bead (see Section 3.5).

For the detection laser (Fig. 14.2, panel 3b), we use an 850 nm, 30 mW diode laser (TECIRL-30GC-850, World Star Tech) which has ∼0.5%

power stability and a measured $\sim$1 μrad pointing stability ($\sim$1 nm in the sample plane, measured over 300 s). This economical laser in our hands achieved much higher pointing stability than actually indicated in its specification ($<$25 μrad). We strongly recommend testing the pointing stability of any laser before use. Sub-μrad stability can be achieved with fiber coupling (Bustamante *et al.*, 2007). The wavelength of the detection laser is selected close to the maximum sensitivity of our PSD model ($\sim$850 nm), which in turn minimizes interference with trapping. The power output of the laser is adjusted using a neutral density (ND) filter (ND3 in Fig. 14.2) to minimize the effect of laser power on trap stability while providing sufficient signal to noise for accurate detection.

3.2.7. Dichroic mirrors
Multiple dichroic mirrors are used in our optical trap layout. Careful consideration needs to be given to the cutoff frequencies of these dichroics to avoid unwanted beam leakage or attenuation. We use five dichroic mirrors in the setup (Fig. 14.2), and they are all purchased from Chroma Technology. Specific model numbers are provided in Table 14.1.

3.3. Noise and stability considerations

Noise is random changes in bead position arising from Brownian motion and unintended fluctuations in the instrument. Brownian motion sets limits on the relative spatial and temporal resolutions of an optical trap (Moffitt *et al.*, 2006, 2008). Brownian motion of biomolecules is a function of solution temperature and cannot be avoided. In fact, the variance in bead position arising from the Brownian motion can be used to calculate the stiffness of the optical trap for a given size and shape of bead (based on the equipartition theorem). Changes in the characteristic Brownian motion pattern are used to discern events of interest in the three-bead assay, as described in the experimental procedures section (Section 4).

Noise arising from unintended fluctuations in the instrument is referred to as instrument noise, and every effort to minimize this noise improves the accuracy and resolution of the optical trap. Instrument noise broadly includes environmental noise (mechanical vibrations, air fluctuations, thermal expansion) and electrical noise (60 Hz noise and ground fluctuation). For a detailed description of techniques to identify and minimize instrument noise, we refer the reader to Bustamante *et al.* (2007). Here, we discuss representative instrumental noise sources in our instrument and suggest simple but useful remedies to minimize them. Identifying and minimizing the noise sources are sufficient to set up a functional dual-beam optical trap that can be used to study myosins with stroke sizes of $\sim$10 nm at $\sim$10 ms time resolution.

3.3.1. Mechanical vibration of the instrument derived from external vibration sources

(a) Set up the optical trap in a room isolated from vibrations (away from equipment with moving parts such as a centrifuges or an elevator). Optical traps are usually built in the basements of building to further minimize vibrations. The air flow in the room needs to be significantly damped.

(b) Use a heavy floated optical table to isolate the trapping components from all external vibration sources. We are currently using a heavy table (784–35631-01, Technical Manufacturing Corporation; resonance frequency ~ 200 Hz) which is floated on air dampers (Gimbal Piston Isolators, Technical Manufacturing Corporation; resonance frequency below ~ 2 Hz).

(c) Do not mount any equipment with moving parts on the optical table. For example, we mount the body of the trapping laser, piezo stage controller, and other motion controllers away from the table.

(d) Use thick ($D = 1$ in.) and short ($L = 2$ in.) posts for the mounting of the optics including mirrors and lenses. Keep the optical beam close to the optical table (height $= 3$ in.) and the total beam path from the lasers to the detector as short as possible.

(e) Build or purchase a stable microscope body with acceptable vibration amplitude and stage drift in your measurement time. Alternatively, use active feedback control of the sample stage using a piezo stage modulation if necessary (Carter *et al.*, 2009; Nugent-Glandorf and Perkins, 2004).

(f) The effect of pointing fluctuations on the trapping laser can be minimized by using the same laser for both traps and by minimizing the distance over which the dual-beam paths are separated. In our current design, this distance between PBS2 and PBS3 is 4 in.

3.3.2. Pointing and power fluctuation of the trap and detection beam

(a) Use lasers with excellent pointing stability (~ 1 μrad or better), power stability (< 1–2%), and beam profile ($M^2 < 1.1$).

(b) Set an isolator right after the trapping/detection beam that blocks the back-reflected beam to the laser, thereby improving power stability.

(c) Use fiber coupling for improving pointing stability, and use active feedback control of an acousto-optic modulator (AOM) for power stability (Carter *et al.*, 2009; Nugent-Glandorf and Perkins, 2004).

3.3.3. Air fluctuation

(a) Enclose the optical beam path in a plexiglass or a plastic box (~ 0.5 in.) to minimize noise due to the air fluctuations. Minimize the total volume occupied by the beam path, as this also minimizes noise from convection currents.

(b) Have all beam paths pass through plastic tubes, especially the beam-focusing spots (between L1 and L2, L3 and L4) where the contribution of air fluctuation is amplified.
(c) Use lenses with short focal length to minimize the beam path. Larger beam paths have disproportionately higher noise than shorter beam paths.

3.3.4. Thermal expansion

(a) During the experiment, do not touch any optical components. Use controllers which are mounted out of the optical table.
(b) Perform optical trapping in a temperature-controlled room (Bustamante *et al.*, 2007; Carter *et al.*, 2009; Lang *et al.*, 2002; Peterman *et al.*, 2003).

3.3.5. Beam quality in the sample plane

(a) Use lasers with good Gaussian beam profile $M^2 < 1.1$. Test the beam profile of the laser before purchase (see alignment protocol). In our experience, even lasers from reliable vendors have significant variability from unit to unit. Testing this parameter can save significant time and effort in set up and alignment of the instrument.
(b) Prevent beam clipping at any optical components (such as lenses, mirrors, AOD, shutters, or irises).
(c) Expand the beam to a final size that is comparable with the aperture diameter of the OBJ.
(d) Select optics with appropriate antireflection coating.
(e) Do not use lenses with a focal length that is too short ($f < 25$ mm). Spherical aberration increases as $\sim 1/f^3$.
(f) Keep optics free from dirt and dust. If you have to clean the optics, follow the recommended method from the manufacturers.

3.3.6. Electrical noise of data acquisition

(a) Ground the optical table by connecting it to a well-characterized building ground. This minimizes static build-up that could interfere with electrical components.
(b) Avoid ground loop by using a different power supply for each PSD and a floating mode for the input channels of the NI-DAQ connector block.
(c) Minimize ambient light to the detector to avoid 60 Hz noise.

3.4. Alignment protocol

Construction of a dual-beam optical trap for the three-bead assay requires alignment of many components as shown in Fig. 14.2. Here, we describe a detailed procedure for the construction of a dual-beam trap in a step-by-step manner. Modules for alignment are as follows—Step 1: bright-field setup for testing the stability of the microscope; Step 2: single-beam trap; Step 3: dual-beam trap for the three-bead assay. Other useful alignment procedures are found elsewhere (Block, 1998; Bustamante *et al.*, 2007; Lee *et al.*, 2007; Spudich *et al.*, 2007).

Step 1 Bright-field setup for checking the stability of the microscope (follow the green arrow in Fig. 14.3A)

An essential first step is the alignment of the bright-field path, independent of the trapping laser, to test the stability of the microscope body. The stability of the microscope is critical for trapping experiments in general, with specific emphasis on reduced noise for the three-bead assay. A measure of stability is the absence of significant fluctuation or drift effects over the time scale of the experiment. The steps involved in this alignment are (1) set up of components, (2) alignment procedure, and (3) testing. For a conventional microscope whose microscope body is already in place, the reader can skip steps (1) and (2).

(1) Position all the components in the bright-field beam path from the LED light source to the CCD as shown in Fig. 14.3A (see the figure legend for the green arrow path for distance and product specifications).
(2) Alignment:
    (a) Adjust the vertical axis of the LED, L6, and M7 to coarsely coincide with the principal axis of OBJ as shown in Fig. 14.3A. This is accomplished by using the holes in the breadboard as a guide to identify the vertical axis, with components positioned 3.5 in. away from the board.
    (b) Align the vertical axis of the z-translation stage of CON such that it coincides with the fixed principal axis of the OBJ. This is done with the LED turned off. Use a spirit-level for angular adjustment of the CON vertical axis. You have to first check that the optical table and the microscope stage are also leveled. Peer down the CON to see the OBJ with transmitted ambient light. Try to coincide the principal axes of OBJ and CON by lateral translation of the CON. The alignment of CON is completed when the z-translation of the stage produces symmetric changes in the shape of the OBJ front face seen through the back aperture of CON (by eye).
    (c) Turn on the LED. Adjust the position and angle of LED and L6 such that the beam passes through the center of the back aperture of CON. Since 740 nm is visible (far red), the beam path can be

checked using plain paper. For this check, create a film of immersion oil between OBJ and CON. Avoid direct contact between OBJ and CON faces as this could damage the lenses.

(d) The beam should be incident at the center of M7 (Fig. 14.3A). Adjust the angle of M7 and M9 (Fig. 14.2) using the knobs of the mirror mount to make the reflected beam parallel to both the table and a row of threaded holes on the table. Adjust the height of L7 and CCD1 to center them along the beam path. Using an infinity corrected objective, L7 can be positioned anywhere in the beam path followed by the CCD1 at the focal point ($f_{L7} = 200$ mm). Move CON or OBJ along the axial direction (be careful not to damage the lenses by direct contact), and view the beam shape on CCD1. If the beam expands and shrinks symmetrically with a fixed center, you are ready to test the stability of the microscope.

(3) The stability can be tested by recording a bright–field movie of beads adsorbed to a coverslip or a calibration slide (5 μm scale or less).

(a) Place a sample channel that has platform beads (diameter~1.5 μm) on the surface of the coverslip between OBJ and CON. Turn on the LED. The LED output power needs to be adjusted using a variable ND filter (ND1) to avoid saturating CCD1. Adjust the z position of OBJ and CON to visualize the bead images on CCD1. Move the OBJ in the z-direction to focus and defocus the bead image. Check any asymmetry or aberration in the bead image (Fig. 14.5B).

(b) Record the image on the CCD camera with appropriate driver software for ~10 min to test the stability of the microscope system. Measure the fluctuation and drift of the center of the beads. If drift is <100 nm over 10 min, the microscope setup should be stable enough to start the trapping beam alignment. Otherwise refer back to Section 3.3 on how to improve the stability of the setup.

Step 2 Alignment of a single–beam trap

Alignment of a single–beam trap consists of the following steps: (1) measuring beam profile and stability of the trapping laser; (2) mounting the trapping laser and an isolator; (3) steering the beam parallel to the optical table; (4) setting up a beam dump to control the power of the trapping beam; (5) setting up the overall beam layout; (6) adjusting the beam path through the microscope objective (OBJ) and condenser (CON); (7) setting up lenses L3 and L4 for beam expansion and coarse beam steering; (8) setting up lenses L1 and L2 for beam expansion and fine beam steering; (9) setting up the AOD for feedback control; (10) setting up OBJ and CON; (11) aligning the bright–field light path; (12) testing the single–beam trap; (13) setting up PSD1 for the back focal plane detection.

To visualize the trapping beam during the alignment, we use IR cards (F–IRC2-S, Newport). During the alignment procedure, it is important to attenuate the beam power to < 50 mW to prevent damage to the IR cards and avoid accidental laser damage to the user and equipment. Note that aligning M1 and M2 (Fig. 14.3B) is done by attenuating laser output directly from the power source. For subsequent alignment steps the laser output is set to high power (> 1 W) for improved beam stability, with a beam dump (HP1 and PBS1 in Fig. 14.3B) to attenuate laser power.

(1) *Measuring beam profile and stability of the trapping laser*

   Beam profile, collimation, and laser stability are usually quoted by the manufacturer in the laser specification sheet. Desired specifications include beam profile $M^2 < 1.1$, power fluctuations to $< 2\%$, and pointing stability of the laser beam of ~ 1 μrad or less. It is important to conduct a quick assessment of the laser beam profile, collimation, pointing, and power stability before use to guard against manufacturing defects or damage during the transportation or handling. The beam profile can be characterized using various tools, including a commercial beam profiler, a knife-edge technique, and an iris technique (Bustamante *et al.*, 2007). Laser stability includes power stability and pointing stability. As a first approximation, power stability can be evaluated by monitoring the power output on a power meter over several minutes (short-term measure) to an hour (long-term measure). Pointing stability is assessed by directing the laser output, after attenuation, to a PSD with a path length of a couple of meters from the laser. PSD output is monitored over time and < 1 μm change in laser position over several minutes suggests good pointing stability. Please note that these measurements must be made with an attenuated beam (use a polarizing beam splitter followed by a beam dump or a ND filter) with power below the damage threshold of the detector. Collimation of the beam can be tested by measuring the beam diameter at multiple distances from the laser.

(2) *Mounting the trapping laser and an isolator*

   Mount the fiber output of the trapping laser (1064 nm, 5 W) followed by an isolator (ISO1) on an optical table (Fig. 14.2, panel 1). The body of the trapping laser is kept off the optical table to minimize vibrations from the power source. Mounting stability of the output fiber of the laser beam affects overall stability of the optical trap. To ensure stable output we use a stable mount (VB–1, Newport) with 1 in. diameter post. The beam path shown in Fig. 14.3B is at a constant height of 3 in. above the optical table to minimize aberrations and simplify the alignment procedure. To minimize beam fluctuations from mechanical vibrations, posts with 2 in. height and 1 in. diameter have been used for most of the mirror mounts. We use an adjustable

tilt mount (KM100, Thorlabs) to run all collimated beams parallel to the surface of the optical table, along the threaded holes. If the beam collimation is not acceptable (>mrad), set two lenses followed by ISO1 to make the beam collimated. Divergence of the laser beam can be identified by measuring the beam diameter several meters away from the beam output.

(3) *Steering the beam parallel to the optical table*

Steering the beam parallel to the optical table is achieved by *walking the beam* using two mirrors M1 and M2 and a set of irises. Set up the two mirrors M1 and M2 (Fig. 14.3B). Prepare the two irises with centers at the same height (3 in. above the optical table). Locate them along the optical table such that they follow the optical path from M2 to M3 (Fig. 14.3B). Locate the first iris close to M2 and the second one >1 m from it. Adjust the position and the horizontal angle of M2 such that the beam passes through the two irises when they are both completely open (0.5 in. diameter). (i) Adjust the angle of M1 making the beam passes through the center of the first iris when it is closed (∼1 mm diameter). (ii) Open the first iris and adjust the angle of M2 to make the beam passes through the center of the second iris when it is closed (∼1 mm diameter). Iterate between (i) and (ii) until the beam passes through both irises when they are closed. When the alignment step is completed, the beam will be parallel to the optical table, 3 in. above it.

(4) *Setting up a beam dump to control the power of the trapping beam*

Mount a half-wave plate (HP1) followed by a PBS1 (Fig. 14.3B). Use HP1 to control the power rather than changing the power of the initial beam to avoid fluctuations in laser output when operating at low power (<1 W). During the alignment, limit the power downstream of the PBS1 to <50 mW for safety. Following alignment, this power can be increased by changing the setting of HP1. The beam diverted to the beam dump can be used for feedback control of a single beam, as described in Section A.2.

(5) *Setting up the overall beam layout*

Set M3–M6 and PM1 using the procedure described in (3) to make the overall beam path parallel to the table (3 in. height) (Fig. 14.3B). The distance between these mirrors is determined by the focal lengths of the lenses L1–L4. We use the *4f arrangement* to create a set of conjugate planes (optical elements highlighted in green dotted lines in Figs. 14.2 and 14.4) to steer the beam efficiently. For the description of the *4f arrangement*, we refer the readers to Bustamante *et al*. (2007) and Lee *et al*. (2007).

For instance, to conjugate the AOD and PM1, the length of the optical path between them is set to twice the sum of the focal lengths of L1 and L2 ($2 \times (f_{L1} + f_{L2}) \sim 24$ in. in our layout),

positioning L1 and L2 at their focal distance from the AOD and PM1, respectively. Similarly, to conjugate PM1 and the back aperture of OBJ, the length of the optical path between them is set to $2 \times (f_{L3} + f_{L4})$ ($\sim$36 in. in our layout), and L3 and L4 are located at their focal distance from PM1 and OBJ, respectively. The lens combinations L1 + L2 and L3 + L4 make up two telescopes that are used to expand the beam from its initial size ($\sim$1.6 mm from fiber output) to overfill the back aperture by $\sim$10% ($\sim$9.6 mm at back aperture). The focal lengths of L1–L4 are selected to minimize beam distortion from spherical aberrations (small focal lengths) and air fluctuations (large focal lengths).

(6) *Adjusting the beam path through the microscope objective (OBJ) and condenser (CON)*

Remove OBJ and CON. Lay a partial mirror ($\sim$90% transmittance) flat on the shoulder of the OBJ mounting thread. A coverglass also can be used instead of a partial mirror. First, adjust the angle of M6 to make the beam pass through the center of the OBJ mounting thread. Second, adjust the angle of DM1 to make the beam reflected by the partial mirror overlap with the incident trapping beam. Iterations between these two steps are necessary to produce overlap.

An IR card with a small hole ($\sim$3 mm) in it can be used to check for overlap. Place the IR card between M6 and DM1. Allow the incident trapping beam to pass through the hole. The beam reflected by the partial mirror will be detected by the surface of the IR card. When the trapping and reflected beams overlap, the reflected beam will not be seen on the IR card surface.

Locate the position of the transmitted beam on the ceiling above the objective mount surface using an IR card. Mark the position of the transmitted beam on the ceiling (to be used for subsequent steps). When the transmitted and reflected beams overlap, the beam path is should be coincident with the optical axis of the objective lens. This is an essential condition for a stable optical trap with Gaussian beam profile at the sample plane. Confirm the coincidence by temporarily mounting the OBJ and checking the transmission of the beam through the OBJ. Orientation of the diverging beam can be checked using the IR card.

(7) *Setting up lenses L3 and L4 for beam expansion and coarse beam steering*

PM1 and the back aperture of OBJ are optically conjugated using *4f arrangement*. When this criterion is satisfied, changes in the trapping beam angle using PM1 rotate the incident beam angle at the back aperture of OBJ, which in turn translates the focused trapping beam in the sample plane. To satisfy this requirement, separation between PM1, L3, L4, and OBJ should be f_{L3}, $f_{L3} + f_{L4}$, and f_{L4}, respectively. This can be achieved in the following steps.

(a) Place L4 at f_{L4} from the temporarily mounted OBJ. Adjust the position of L4 to direct the transmitted beam to the mark on the ceiling with minimum beam size. When the beam size is minimized, L4 is position at its focal distance from the back aperture of the OBJ.

(b) Remove OBJ and put the partial mirror back on the mounting shoulder. Place an iris (Iris2) between PM1 and L4 at f_{L4} from L4 (Figs. 14.3B and 14.4). Adjust the position of Iris2 such that the trapping beam passes through the center of it (use IR card). Close Iris2 and insert L3 at distance f_{L3} from Iris2. Adjust the position of L3 such that the power of the beam transmitted through Iris2 is maximized. Open Iris2. Adjust L3 such that the transmitted beam arrives at the mark on the ceiling. Also, check the collimation of the beam by looking at the beam size at a long distance (>3 m). Translate L3 in the beam direction to achieve well–collimated beam, if necessary.

(c) Check whether the distance between PM1 and L3 is still f_{L3}. If the error is not negligible (>10 mm), adjust the location of PM1 and M5 to achieve this condition. If adjustment of PM1 or M5 is required, go back to Step 2.5 and iterate through all the steps to make satisfy all conditions.

(d) Fine adjustment of the position of L3 and L4 is done as follows. (i) Adjust the position of L3 such that the beam transmitted through the objective mount arrives at the position marked on the ceiling (see Step 2.6). (ii) Adjust the position of L4 such that the beam reflected by the partial mirror (see above using an IR card with a hole) coincides with the trapping beam. Iterate between (i) and (ii) until both conditions are satisfied.

(e) Now, PM1 and the back aperture of OBJ should be optically conjugated. When this criterion is satisfied, changes in the trapping beam angle using PM1 should not translate the beam position at the back aperture of OBJ. Rotate PM1 and confirm that all deflected beams arrive at the center of the OBJ thread. Also, check the beam diameter of the final beam size whether it is the same with the calculation (4.8 mm in our layout).

(8) *Setting up lenses L1 and L2 for beam expansion and fine beam steering*

(a) Between M4 and M5, set Iris1 at $2 \times f_{L2}$ from PM1, L1 at f_{L1} from the Iris1, and L2 at f_{L2} from PM1 (Figs. 14.3B and 14.4). Follow the procedure described in (7e) to adjust the position of L1 and L2 such that the transmitted beam is directed to the mark on the ceiling and the reflected beam by the partial mirror is coincident with the incident trapping beam.

(b) Insert a coverslip (No. 1 size on a mirror mount) between M3 and PBS1 at an angle of $45°$ with the incident trapping beam path.

Look at the beam size of the back–reflected beam (reflection from partial mirror) at a long distance (>1 m). If the beam size is comparable with the initial laser output beam, the trapping beam is sufficiently collimated at the OBJ back aperture. If the beam is much larger than the initial beam, translate L1 in the beam axis such that the back–reflected beam size is minimized. Check whether the final beam size ~ 9.6 mm such that the final beam barely overfills the back aperture of the OBJ.

(9) *Setting up the AOD for feedback control*

    (a) Fast (10 kHz) beam steering and feedback control of the trap can be achieved using an AOD. Place an X–AOD (Figs. 14.2, 14.3B, and 14.4) such that its back face is positioned f_{L1} from L1. Please note that the XY–AODs should be mounted on a one-axis translator to change the path length between the AOD and L1 (used for conjugating AOD and PM1). A custom-built Labview program feeds an RF signal to the AOD that changes the angle of the first-order diffraction. Set the frequency of the RF signal to the center frequency recommended by the manufacturer. You will find multiple diffraction spots (only two spots are usually bright enough to be seen on an IR card) at the front focal point of L1. Use Iris1 at this location to transmit only the first-order diffracted beam (Fig. 14.4). Adjust the position and angle of the X–AOD to maximize the power of the first-order diffracted beam (use power meter). Place a Y–AOD such that its front face is positioned at f_{L1} from L1, so the X–AOD and the Y–AOD are very close to each other. Now, you will see four spots clearly before Iris1. Adjust the position of Iris1 to choose only the beam that is first-order diffracted by both AODs. The first-order diffracted beam from both AODs can be identified by turning the X– and Y–AODs on and off. Adjust the position and angle of Y–AOD as done for X–AOD to maximize power output.

    (b) When AOD and PM1 are optically conjugated, the first-order diffracted beam will be incident at the center of PM1. Also, with the Iris1 between AOD and L1 open, all beams transmitted through the AOD should arrive at the same spot at PM1. Use translators to move the AODs along the optical path to alter the position of the AOD along the optical path between M4 and L1 to satisfy these two conditions.

    (c) Setting AOD will change the incident beam (first-order diffracted beam) angle into the OBJ. Rotate the angle of PM1 such that the partially back-reflected beam again overlaps with the incident beam.

(10) *Setting up OBJ and CON*

    (a) Mount the OBJ and CON. Place a film of immersion oil between the OBJ and CON. Adjust the position of the CON such that the

beam transmitted through it is collimated (use an IR card far (>1 m) from the back aperture of the CON). Note that the transmitted beam size from the CON could be different from the incident beam depending on the model of the CON. The aperture size of our CON model is ∼20 mm. Adjust the position of CON to make the transmitted beam coincide with the mark on the ceiling.

(b) The axes of the trapping beam, OBJ, and CON need to be coincident. To achieve this, we use the procedure described later. Note that with this technique we can also detect aberrations in shape of the beam incident at the back aperture of the OBJ. Move the CON away from the OBJ such that the beam is slightly converging. Place a CCD camera roughly at the focal point of this converging beam (use ND filters to attenuate the beam power below the CCD damage threshold of the CCD). You will notice an airy pattern as shown in Fig. 14.5A. Moving the CON up and down should expand and contract the size of this pattern. Adjust the position of the CON such that the beam expands and contracts symmetrically. Remove the CCD after this alignment step.

(11) *Aligning the bright-field light path*

Make a sample channel that contains both platform beads (diameter ∼1.5 μm) on the coverslip and freely diffusing beads for trapping (diameter ∼1 μm). Put immersion oil on both sides of the channel. Mount the channel between OBJ and CON. Turn on the LED (740 nm) and adjust the OBJ height to make a bright–field image of the sample plane on CCD1. Adjust the positions of the LED and L6 such that they are centered on the transmitted trapping beam. Adjust the positions of L7 and CCD1 to obtain a focused bright-field image of the sample channel (Fig. 14.5B). Adjust the height of OBJ such that the beam is focused near the interface of water and glass. Turn off the LED. If the trap is within the field of view of OBJ and the sample plane is close to the glass surface, the back-reflection of the trapping beam at the glass–water interface will be visible on CCD1. Adjust the position of CCD1 and L7 such that this back-reflected beam is at the center of the field of view. The back-reflected beam is visible as an interference pattern on CCD1, which expands and contracts in size with up–down motion of the OBJ. If the trap is correctly aligned, this interference pattern is symmetric in shape (similar to Fig. 14.5A). Note that the back–reflected beam can be used at any stage to locate the position of the trap in the field of view.

(12) *Testing the single-beam trap*

Turn on the LED. Move up the OBJ such that the trapping beam is focused in the aqueous solution. Beads that are located close to the surface appear dark at their center (Fig. 14.5B), whereas beads far away

from the surface are light at their center (not shown). Note that only beads between the trap and the coverslip surface (dark center) can be trapped. Beads further in solution than the trap will be pushed away from the trap center by the radiation pressure of the trapping beam.

Increase the power in the trapping beam to ~ 50 mW at the back aperture of OBJ. This can be done by turning up the laser power and/ or by using HP1. Try trapping a bead with a dark center by moving the $x-y$ translation stage. Once a bead is trapped, move it using PM1 to test the stability of the trapping beam. If the trap is aligned correctly, the bead should move in response to changes in PM1. An unstable trap is usually a consequence of low power at the back aperture of OBJ, improper alignment of the trap, clipping of the trapping beam at the back aperture of OBJ, or a distorted trapping beam shape. Check all these possibilities if necessary.

(13) *Setting up PSD1 for back focal plane detection*

(a) PSD1 needs to be optically conjugated with the back focal plane of the CON. To achieve this, place DM2, L5 ($f_{L5} = 75$ mm), and a CCD (in place of PSD1) as shown in Figs. 14.3A and 14.4. Distances between the back focal plane of CON, L5, and CCD are 230 and 110 mm, respectively, which satisfies the condition $1/230 + 1/110 \sim 1/75$. The size of the CON aperture is ~ 20 mm, whereas the size of PSD1 is 10 mm. Hence, we demagnify the beam size twofold ($M = 110/230 \sim 0.5$). Collimate the transmitted beam by adjusting height of the CON. Adjust the position of L5 and the CCD such that the transmitted beam is directed on the center of the CCD. The position of the CCD is optically conjugated with PM1, and the back focal plane of OBJ and CON. Thus, rotation of PM1 should not move the transmitted beam position on the CCD. Test this by steering PM1. If the beam moves with PM1, adjust the position of the CCD along the beam path to minimize this translation.

(b) Visualize the back-focal plane interference pattern of a bead using the CCD. This can be done using either a platform bead or a trapped bead. Test a platform bead first by moving the trapping beam (use PM1) to the center of a bead. Use the back–reflection of the trapping beam (see (11)). When the beam is focused near the center of the bead, you will see a dark interference pattern at the center of the image as shown in Fig. 14.5C. Changing the relative position of the trapping beam and the platform bead will change the interference pattern, as shown in Fig. 14.5C. Now visualize the interference pattern of a trapped bead. You will see fluctuations in the shape of the interference pattern, which reflects the Brownian motion of the trapped bead.

(c) Design a stable box for mounting the PSD on the breadboard (Fig. 14.3A). It is important to avoid ground loops with multiple

devices connected to the same ground line. This is avoided by using a different power supply unit for each PSD. The optical table surface must also be grounded to prevent electrostatic problems.

(d) Move the trapping beam to the center of the platform bead as done in (b), such that a dark interference pattern as shown in Fig. 14.5C (center panel) is visible. PSD1 is put in place of the CCD (the detection surface of the PSD should be at the same position as that of the CCD). PSD1 is linked to a National Instruments data acquisition card (NI-DAQ) connected to a personal computer, which runs a custom Labview program and records the four voltage outputs from the PSD (x, y, sum_x, and sum_y). Move the platform bead by known discrete ($\sim$nm) steps using the piezo stage and measure the corresponding normalized voltage change (x/sum_x and y/sum_y). A linear regression fit to these measurements yields the conversion factor (in Δvolts/Δ nm). Record the signal from the platform bead to estimate the noise voltage level. The noise voltage is a measure of the spatial resolution of the trap. Noise voltage can be reduced, if necessary, by techniques discussed in Section 3.3. Power spectrum analysis can be used to pinpoint the main noise source. Once the PSD setup is completed, the single-beam trap is ready for use, following calibration of the AOD, PSD, and trap stiffness (see Section 3.5).

Step 3 Dual-beam trap for the three-bead assay (Fig. 14.2)

Transitioning from a single-beam optical trap to a dual-beam setup is straightforward and is described here. The dual-beam trap requires two independent trapping and detection beams for the two trapped beads. These are obtained by using p- and s-polarized components of the trapping and detection laser beams (Fig. 14.2, panel 1 and 3b). For the second trapping beam path, we add HP2, PBS2, PM2, and PBS3 (Fig. 14.2, panel 1). For detecting the position of the additional bead, we add PBS4, L13, and PSD2 (Fig. 14.2, panel 3a). To illuminate and image the actin filament, we set up a fluorescence laser (532 nm) and CCD2 camera, respectively (Fig. 14.2, panel 5). The laser wavelength is a function of the specific fluorescent phalloidin conjugate used to label the actin filament. The 532 nm laser and corresponding optical components are shown by way of an example for TMR–phalloidin conjugate. When the actin dumbbell is stretched taut, the bead is no longer at the center of the optical trap, and therefore could be outside the linear range of the PSDs. Hence, we recommend the setup of an additional detection laser beam path (Fig. 14.2, panel 3b) for studies that use the dual-beam optical trap for the three-bead myosin assay described here.

(1) *Setting up a second trapping beam path for the dual-beam trap*
   (a) Add HP2, PBS2, PBS3, and PM2 to create the second beam path
       of the dual–beam optical trap (Fig. 14.2, panel 1). HP2 and PBS2
       split the p- and s-polarized components of the trapping beam. PM1
       and PM2 steer the two trapping beams independently of each
       other. PBS3 combines the s- and p-polarized trapping beams.
       The relative power (trap stiffness) of the two laser traps can be
       adjusted by rotating the angle of HP2. For the dual-beam assay, the
       angle of HP2 is adjusted to equalize the trapping power in both
       trapping beams.
   (b) To align the second trapping beam, roughly adjust the angle of
       PM2 such that the second beam (s-polarized) overlaps with the first
       beam (p-polarized). Fine adjustment can then be done as follows.
       (i) Adjust the angle of PM2 to overlap the two beams at a position
       between M6 and L4 (use IR card). (ii) Adjust the angle of PBS3 to
       overlap the two beams at the position between L4 and DM1 (use
       IR card). (iii) Iterate between (i) and (ii) until both conditions are
       satisfied.
   (c) Once the two trapping beams are coupled, the dual–beam trap can
       be tested using a bright-field image on CCD1. Set up a sample
       channel that has both platform beads and trapping beads. Adjust the
       height of OBJ such that the platform beads are in focus. Two back-
       reflected trapping beams (reflected at the interface between the
       water and the glass coverslip) should be seen using CCD1. PM1
       and PM2 can be used to position the trapping beams 5–10 μm from
       each other, at the center of the CCD1 field. The x–y stage is used
       to trap the two beads, one in each trap.
(2) *Setting up additional components to detect the position of the second
    trapped bead*
       Each of the two trapping beams can be used for back focal plane
    detection of the corresponding trapping bead position. Since the dual
    trapping beams are orthogonally polarized (s and p), the two transmit-
    ted beams can be separated using PBS4. Set PBS4, L13, and the PSD2 as
    seen in Fig. 14.3A. Adjust the position of PSD2 such that the transmit-
    ted beam arrives at the center of the position sensor (use IR card). The
    distance between PBS4 and PSD2 should be identical with that
    between PBS4 and PSD1, to ensure that PSD2 is conjugated with the
    back aperture of CON.
(3) *Setting up a detection laser beam path for the three-bead myosin assay*
   (a) As previously mentioned, an additional detection laser (850 nm) is
       necessary to ensure linear response of the back focal plane detection
       technique. The procedure to align the detection beam path is similar
       to that of the trapping beam path. Place the detection laser, M8,
       PM3, and DM5 as shown in Fig. 14.2. We need to optically

conjugate PM3 with the back aperture of OBJ. To ensure this, the distance between PM3 and L4 is set equal to the distance between PM1 and L4 (500 mm). We need to couple the detection and trapping beams. This can be done by walking the detection beam by adjusting PM3 and DM5 with the trapping beam as a guide.

(b) Set up L8–L10 as done in the previous trapping beam alignment step (Step 2, lenses L1–L4). In each instance, the detection beam is to be aligned to the trapping beam. To ensure that PM3 is optically conjugated with the back aperture of OBJ, lens L10 is selected to have the same focal length as L3. The focal length of lenses L8 and L9 is selected to expand the detection laser beam to slightly overfill the back aperture of the OBJ ($\sim$9.6 mm). Note that the distance between L10 and L4 is the same as that between L3 and L4 (400 mm). To ensure that the detection beam is collimated, translate L8 or L9 parallel to the beam path. PM3 and PSD1 are optically conjugated if changes in angle of PM3 do not translate the beam at PSD1. To satisfy this, L10 can be translated parallel to the beam path. Subsequently, translate L8 or L9 to ensure that the detection beam is collimated with appropriate beam size.

(c) A second detection beam is generated by adding HP3, PBS5, PBS6, and PM4. The alignment procedure is the same as that for the second trapping beam path (Step 3.1a–b).

(d) Make a sample channel that has both platform and trapping beads. Now, you will see four back-reflected beams (reflected at the interface of water and glass coverslip) on CCD1, two from the trapping beams, and two from the detection beams. By controlling PM3 and PM4, overlap the detection beams with their corresponding trapping beams on CCD1 (PM1–PM3 and PM2–PM4).

(e) Use an ND filter (ND3) at the output of the detection laser (Fig. 14.2, panel 3b) to attenuate the detection beam power at the PSD to a few mW. This is done to optimize the sensitivity of the PSD output. Place a bandpass filter (F1) to block the 1064 nm trapping beam and transmit the 850 nm detection beam. Alternatively, a notch filter that blocks 1064 nm trapping beam also can be used for the filtering. Mount F1 on flipping mirror mounts such that the transition between the trapping beam- and detection beam–based measurement of the bead position is easily achieved.

(f) Trap beads in both traps. The PSD output reflects the Brownian motion of the trapped beads. You can estimate the noise level in the detection beam using a platform bead, as done in Step 2.13d.

(g) (Optional) Set up two shutters between PBS2 and PBS3 for each beam path (shown in Fig. 14.2, not shown in Fig. 14.3) to turn on/ off each trapping beam independently. This is useful for making an actin dumbbell. See Section 4.1.

(4) *Set up for visualizing the actin dumbbell*

A 532 nm laser is used to excite the fluorescent phalloidin bound to the actin filament with the emission being imaged on CCD2 (Fig. 14.2, panel 5). Set up the fluorescence laser (532 nm), DM3, DM4, L11–L12, and CCD2 as seen in Fig. 14.2, panel 5. Expand the initial beam size of the 532 nm laser, if necessary, to expand the field of illumination (not shown in Fig. 14.2). DM3 reflects the excitation beam (532 nm) and transmits the emission beam (580 nm peak). DM4 transmits the 740 nm LED beam to CCD1 for the bright-field image, whereas it reflects the 580 nm emission peak of TMR to CCD2. L11 is positioned at its focal length (f_{L11} = 250 mm) from the OBJ. Using an infinity-corrected objective lens, L12 can be positioned anywhere in the beam path, followed by CCD2 at its focal point (f_{L12} = 200 mm) for the epifluorescence illumination. Attenuate the fluorescence beam using ND2 so that the beam does not damage protein molecules or cause rapid photobleaching of the dye. Adjust the angle of DM4 such that the fields of view of CCD1 and CCD2 are similar. Visualizing both the bright field and the fluorescence images simultaneously facilitates the creation of the actin dumbbell (see Section 4.1).

(5) *Cover the overall setup using tubes and a box*

Once all of the alignment procedure is completed, enclose all of the beam paths in a box and tubes. Use small tubes ($\sim$1 in. diameter) to locally enclose all beam paths, and build a thick plastic box ($\sim$0.5 in. thickness) to globally cover all components. This will significantly reduce the effects of air fluctuations, which is essential for the stable trap.

3.5. Calibration

Calibration of AOD, PSD, and trap stiffness are essential procedures for accurate and precise measurement of nanometer displacements and piconewton forces (pN) generated by a single myosin molecule. For this calibration, we need to know the relationships between the displacement of the trapped bead in the sample plane (nm) versus. (1) changes in the frequency input to the AODs, (2) changes in the output voltage of PSD, and (3) the restoring trap force. Here, we introduce simple methods to quantify these conversion factors. Other methods are also found elsewhere (Berg-Sørensen and Flyvbjerg, 2004; Bustamante *et al.*, 2007; Neuman and Block, 2004).

3.5.1. Conversion of changes in the voltage input to the AODs to bead displacement

Apply a voltage input to the AOD and measure the peak-to-peak displacement of a trapped bead on the bright-field image captured by CCD1. Repeat this with stepwise increases in AOD voltage input. The peak-to-peak displacement is read out in CCD1 pixel units, which can be

converted to nanometer distance by calibrating the CCD1 field of view using a calibration slide (5 μm scale). Use this procedure to obtain a graph of the peak–to–peak displacement (nanometer) against the voltage input of AOD. Use a linear regression fit to the linear part of this graph (assessed visually) to obtain the nanometer bead displacement per volt input voltage at the AOD.

3.5.2. Conversion of changes in voltage output at the PSD to bead displacement

PSD output is merely a voltage signal, so we need a conversion factor for the real displacement of the bead in the sample plane as a function of PSD voltage output. This can be done using back focal interference detection in conjunction with either a trapped bead or a platform bead.

(1) *Using a trapped bead for calibrating the PSD output*

This method is used when a separate detection beam path is used for measuring bead position. First, trap two beads and separate them by ~ 5 μm. Ensure that the trapping and detection beams overlap. This is done by adjusting PM1–PM4 to overlap back-reflections of the trapping and detection beams, observed on CCD1 (for details, see Section 3.4, Step 3.3d). Apply a series of voltage inputs to the AOD to raster scan the CCD field of view and collect the normalized PSD voltage outputs (x/sum_x and y/sum_y). The PSD voltage output file can be used to map PSD voltage to AOD voltage, which in turn can be mapped to bead displacement in the sample plane (Section 3.5.1). Since variance in size and shape of the trapped bead can result in changes of the PSD response, make a mapping file for each bead used in an experiment.

(2) *Using a platform bead for calibrating PSD output*

Use the piezo stage to move the platform bead through a series of displacements across the field of view and record changes in the PSD voltage signal. This also yields a 2D mapping file, similar to (1) that directly converts PSD signal to bead displacement at the sample plane. One drawback of this technique is that the z-position of the platform bead relative to the sample plane varies from bead to bead. A combination of (1) and (2), however, is sufficient for accurate calibration of the PSD output.

3.5.3. Measuring trap stiffness

A number of different methods have been developed to measure trap stiffness (Berg–Sørensen and Flyvbjerg, 2004; Neuman and Block, 2004; Tolic-Norrelykke *et al.*, 2004, 2006). Three representative methods are the equipartition theorem method, the power spectrum method, and the hydrodynamic drag force method (for a detailed description, we refer the reader to Neuman and Block (2004) and Perkins (2009)). Since these are complementary approaches, we recommend using all of them for a better estimate of trap stiffness. Power spectrum analysis is a useful method to determine trap stiffness,

as it dissects all frequency components of the bead movement. See Berg-Sørensen and Flyvbjerg (2004) for theoretical details and Tolic-Norrelykke et al. (2004) for analysis software. In the case of the three-bead assay, tension in the actin dumbbell displaces the bead from the trap center and alters the effective stiffness experienced by the trapped bead in the presence of the actin dumbbell. The trap stiffness is linearly proportional to the local spatial gradient in trapping power. As the trapped bead moves away from the trap center, this gradient increases, thereby increasing the trap stiffness. We find a $\sim$10–20% increase in trap stiffness following the formation of the actin dumbbell (see Section 5.2.1, Step 1 on compliance correction for details on measuring trap stiffness in the presence of the actin dumbbell).

4. OPTICAL TRAPPING EXPERIMENT

In the three-bead assay, an actin filament is stretched taut between two 1 μm diameter polystyrene beads (Fig. 14.1). The actin filament is biotinylated and the polystyrene beads are coated with neutravidin to facilitate the formation of the actin dumbbell (Rief et al., 2000). The coverslip surface is coated with 1.5 μm diameter glass beads, which serve as platforms for the myosin. The coverslips are dipped in 0.1% solution of nitrocellulose in isoamyl acetate and dried overnight. This sticky surface is coated with antibody against green fluorescent protein (GFP). Myosin chimeras are used that have their C-terminal cargo-binding domains replaced by GFP (Rock et al., 2001). Thus, a single molecule of myosin can be positioned on the top of a glass bead platform with its GFP tail domain bound. Since the myosin is anchored to the surface, as the motor strokes the actin filament slides, thereby pushing against one trapped bead while pulling against the other (Fig. 14.7).

Preparation of reagents, including biotinylated actin filaments, platform bead coated coverslips, andr-28-3Tmbnd tin (Spudich et al., 2007). Her-, we discuss the procedure to create a taut actin dumbbell and to test platform beads to find a myosin motor that interacts with the filament and displaces the trapped Start by creating

Sometimes, the trapped beads look asymmetric in shape or are composed of a chunk of multiple beads. Also, some trapped beads are already connected to bundles of actin filaments on the surface. In these cases, close the corresponding shutter and selectively release the bead from its trap.

Remove the beam block and allow the fluorescence laser to illuminate the field of view. Observe actin filaments in solution on CCD2. Translate the x–y stage to bring a single long actin filament (avoid clumps) close to one of the trapped beads. Actin binding to one of the trapped beads can be confirmed by moving the x–y stage. Move the x–y stage parallel to a line connecting the trapped beads, such that the flow caused by this motion brings the actin filament in the vicinity of the second bead. Move the x–y stage perpendicular to the actin filament. If the actin filament is bound to both trapped beads, it will not move away from either trapped bead.

4.2. Tensing the actin dumbbell

Steer the detection beams (PM3 and PM4) so that they overlap with the trapping beams (use back–reflections, see Section 3.4, Step 3.1c). Use PM2 to move the second trapped bead away from the first. Monitor the PSD signals in the direction parallel to the actin filament (for instance, if the actin filament is along the Y-axis, monitor y/sum_y for each PSD). As the actin dumbbell becomes taut, the first trapped bead will begin to move out of the trap center in the bright-field image. At this stage, use small incremental movements to further tense the dumbbell. The PSD outputs reflect the Brownian motion of the two trapped beads. The actin dumbbell is sufficiently taut when the PSD output signals appear correlated in time. It is important to keep repositioning the detection beam during this process to ensure that it coincides with the trapping beam. As the detection beam moves away from the trapping beam, PSD sensitivity, and hence the variance of the PSD output decrease. Reposition the detection beam to maximize variance in the PSD output.

4.3. Testing platforms

Find a single platform bead (avoid doublets or clumps) by steering the x–y stage. The actin dumbbell should be positioned slightly further in solution than the platform beads, to avoid snagging the dumbbell on the surface of the platform bead. Adjust the coverslip height such that the midpoint of the actin dumbbell is at the surface of the platform bead. When an active myosin on the surface of the platform bead interacts with the actin dumbbell, both the variance and mean position of the PSD outputs change (Fig. 14.6).
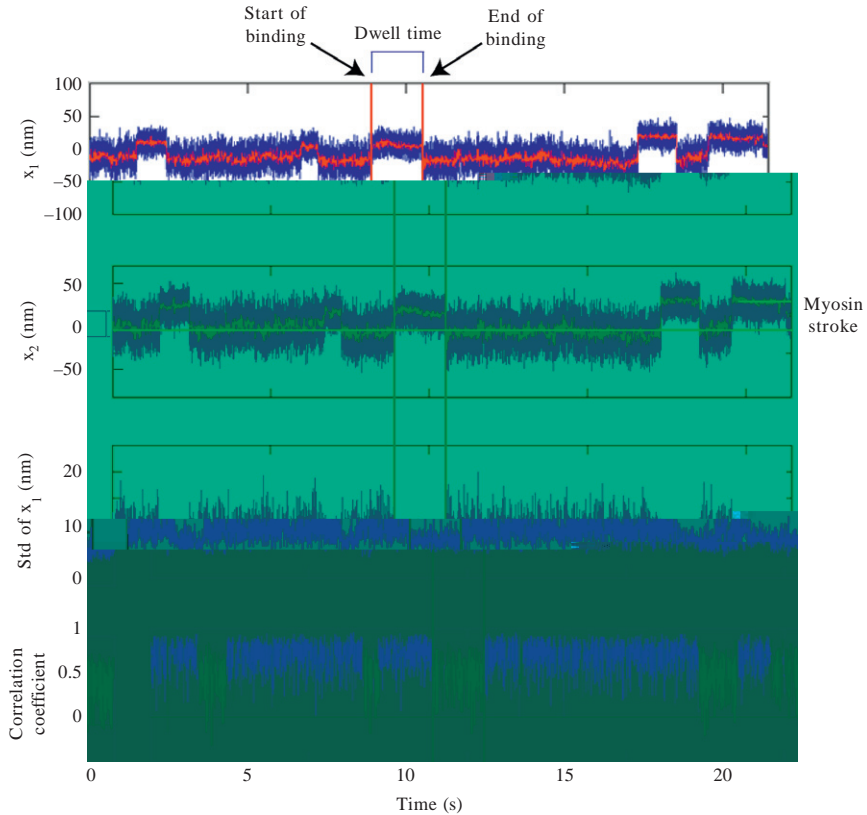
Figure 14.6   Representative experimental result of a nonprocessive motor. The time traces show the interaction of a single-headed myosin VI construct with an actin filament. The first and the second graphs show the time trajectory of the first (x_1) and the second (x_2) bead positions. The blue line shows the raw data with a sampling rate of 10 kHz while the red line is the low-pass filtered result of the raw data (fourth-order low-pass digital Butterworth filter with a cutoff frequency of 50 Hz. The trap stiffness in this particular example is ~0.02 pN/nm, and this results in Brownian motion of bead (blue line) with standard deviation (std) of ~10 nm. Increasing trap stiffness will reduce the std of Brownian fluctuation. In the figure, there are five very clear binding and unbinding events, showing a sudden jump and drop in the bead positions. The duration between binding and unbinding events is the dwell time. The stroke size refers to the displacement of the bead position when the binding event occurs. This stroke size is before compliance correction which is explained in the legend to Fig. 14.7 and in Section A.2. The third and fourth graphs show the std of the first bead position and the correlation coefficient between the two bead positions, respectively. At the third binding event at ~10 s, for example, we observe a sudden drop in the std as well as the correlation between x_1 and x_2. This happens because the myosin binding clamps the actin dumbbell, reducing its Brownian fluctuations, which in turn reduces the Brownian fluctuations of the two trapped beads. We use a custom Matlab program which automatically finds two different states in the correlation graph, so the sudden change of the color (blue and green) in the last graph helps to visualize the binding events. We manually choose the timing of binding and unbinding events based on the std and the correlation. The binding events are chosen only when both the std and the correlation change register a significant change.

4.4. Identifying binding interactions

Lowering the actin dumbbell too far will result in reduced variance in bead movement as a consequence of direct contact with the bead surface. When properly positioned, processive myosins will produce a characteristic staircase pattern. Nonprocessive myosins release the actin before the next binding event. These features can be used to distinguish a properly oriented active platform from a platform that is in direct contact with the actin filament.

Bead displacements that are too close to each other in time or even simultaneous are likely a result of multiple motors on the surface. The motor dilution used should be adjusted so that only one in ten platforms or less interacts with the actin filament. For a detailed discussion of how to avoid multiple motors, see Spudich *et al.* (2007). Before collecting data on a single motor platform, move the actin dumbbell to the side of the bead and increase tension in the dumbbell to obtain good correlation between the two signals. The piezo stage can be used to optimize the motor position such that myosin binds at well-spaced intervals ($\sim$5 s apart).

5. DATA ANALYSIS

The optical trap is a powerful means of discerning the kinetic mechanisms of molecular motors. The processes measured in the optical trap, for

5.1.1. Graphing the data

A common method of portraying dwell time data is as a histogram. This method has several obvious advantages: it is easily interpretable, and is, in principle, readily fit with probability density functions:

$$A \xrightarrow{k} B, \quad f = k e^{-kt}, \tag{14.1}$$

$$A \xrightarrow{k_1} B \xrightarrow{k_2} C, \quad f = \frac{k_1 k_2}{(k_1 - k_2)} \left(e^{-k_2 t} - e^{-k_1 t} \right). \tag{14.2}$$

Here, f is the normalized probably density function for a single process (14.1) or sequential exponential processes (14.2). These two distributions are mentioned in particular because they are by far the most common situations encountered in single–molecule data. Single exponential kinetics result when a single process is much slower than all the other steps in the observed portion of the catalytic cycle. An example is ADP release from myosin V at saturating ATP concentrations. Sequential exponential kinetics occurs when two processes have comparable rates. For example, the rates of ATP binding and ADP release are both $\sim 10 \ s^{-1}$ at 10 μM ATP. It is worth noting that the distinction between these two cases is somewhat arbitrary: It is rare in practice to have a dwell time distribution that truly reflects only one underlying rate. However, it is common to observe kinetics where one process is ~ 10 times slower than all the rest.

Unfortunately, histogramming the data suffers from several drawbacks. The choice of bin size is somewhat arbitrary, and can be massaged such that the data coincide with the anticipated model. Furthermore, each binned data point is often erroneously given equal weight during fitting, despite the low statistical significance of the bins containing only a few (<5) observations. Using variable–width bins can of course alleviate this problem by ensuring that each bin contains at least five observations.

The most serious problem from a practical standpoint is that histogramming necessarily greatly reduces the number of data points being fit with the model. For example, ~ 200 dwell time observations, when histogrammed, will result in only ~ 10–15 bins. This makes it difficult to discern the likely underlying mechanism by visual inspection of the data. The reduction in the ratio of data points to parameters also inflates fit errors when performing a straightforward least-squares fit to the data.

The use of cumulative distributions avoids many of the drawbacks associated with histograms. A common form of the cumulative distribution plots the fraction of dwells that are longer than a given time t. A f(m)10(ul)19(at)19(c)21–25.0070

Fitting to cumulative distributions removes the complexities associated with properly treating binning artifacts: each observation is given equal weight. Further, the ratio of data points to parameters is much higher than in histogrammed data because the data are not collapsed into bins. Imperfections in the data and differences between the data and model are both often more apparent than in histogrammed data. Cumulative distributions are not intellectually exotic: the integrated rate laws are equally applicable to, for instance, data resulting from an analogous stopped–flow experiment in which a synchronized population evolves with time.

A least–squares fit to the dwell time data using commercial software is often used and has a number of immediate practical advantages. It is very easy to implement in numerous software packages, for instance, Matlab (MathWorks) or Igor (WaveMetrics). The fit is sensitive to outliers. Hence, poor-quality data (for instance, a dataset that is missing observations at short dwell times) will result in obviously poor fits. Finally, commercial packages provide numerous statistical measurements of the goodness of fit, for instance, RMSD, χ^2, reduced χ^2, and confidence intervals.

However, reliance on commercial fitting routines suffers from several important drawbacks. First, as discussed later, it is possible and desirable to find the *most likely* values of the fit parameters given one's data, rather than the parameters that result from a nontransparently implemented nonlinear fit. Second, common commercial fitting software often does not take the covariance of fit parameters into account in computing confidence intervals, which can result in severe underestimates of fit uncertainty. Third, least–squares fits do not take sampling error into account. This is a crucial limitation, given the small sample sizes that often characterize single-molecule experiments.

5.1.2. Maximum likelihood estimation

Here, we give a very brief introduction to the fitting method of maximum likelihood estimation, a better fitting method than using least–square fitting (Rao, 1965). Given a collection of dwell times $(t_1, \ldots, t_n)$ and a probability density function f with parameters k $(k_1, \ldots, k_m)$, one may define the likelihood of observing exactly this collection of dwells:

$$P(k, t) \propto \prod_i f(k, t_i). \tag{14.5}$$

In principle, all that is necessary is to find the values of k that maximize P. In practice, it is easier to minimize the negative logarithm:

$$-\log(P(k, t)) \propto \sum_i -\log(f(k, t_i)). \tag{14.6}$$

This minimization can be done using iterative minimization routines that are commonly built into analysis software such as Matlab. However, it is often possible to find the k that minimizes the P analytically by taking the partial derivative with respect to each element in k. Consider the exponential distribution:

$$P(k,t) \propto \prod_i^N k e^{-kt_i}, \tag{14.7}$$

$$\ln(P(k,t)) \propto \sum_i^N (\ln k - kt_i), \tag{14.8}$$

$$\frac{\partial}{\partial k} \ln(P(k,t)) \propto \sum_i^N \left(\frac{1}{k} - t_i \right). \tag{14.9}$$

For convenience, we calculate $\ln(P)$ instead of $-\log(P)$. In order to find the maximum of $\ln(P)$, we set the partial derivative of $\ln(P)$ with respect to k equal to 0:

$$0 = \sum_i^N \left(\frac{1}{k} - t_i \right) = \frac{N}{k} - \sum_i^N t_i,$$

$$\frac{1}{k} = \frac{1}{N} \sum_i^N t_i. \tag{14.10}$$

Equation (14.10) indicates that the most likely estimate for k is simply the inverse of the average dwell time! An analogous, but algebraically messy derivation of maximally likely values of k_1 and k_2 is likewise possible for the sequential exponential function.

The maximum likelihood estimate is, by definition, the best estimate for the given parameter. Further, its value can often be derived analytically, as earlier. Methods to derive fit errors based on maximum likelihood calculations are well established. However, these methods do not account for fit uncertainty introduced by small sample sizes, as discussed later.

5.1.3. The bootstrap method

This very useful but probably less well-known method of data analysis was introduced and popularized by Efron and Tibshirani (1994). The key underlying assumption is that the observations in the dataset are independent: a given dwell time observation is not influenced by the length of the preceding or following dwell. This is most often, but not always, the case.

The bootstrap method further assumes that the data t constitute a representative sample of the underlying distribution. If one were to repeat the experiment and again make N observations, the resulting observed data and fit parameters would be similar. Any differences would stem principally from the finite sizes of the two datasets. The bootstrap method simulates many repetitions of the experiment: from a dataset t containing N observations, a synthetic dataset b is created by randomly selecting N observations from t with replacement. This means that the same t_i may be chosen more than once when creating b. The dataset b is then fit using the method of one's choice resulting in fit parameters k_b. This process is repeated several thousand times, resulting in a set of synthetic fit parameters (k_b).

The beauty of this procedure is that the error for each element k_i in **k** is the standard deviation of corresponding elements in k_b. For example, suppose the data are fit with a single exponential. In order to find the fit uncertainty, the maximum likelihood estimate k_b is calculated for each b. This procedure is then repeated many times. If the data do not suffer from some underlying experimental flaw, the resulting collection of k_b values is approximately normally distributed. The standard deviation of this distribution gives the uncertainty on k.

This approach has several strengths in estimating fit uncertainties. First, it makes no assumptions about the data other than those mentioned earlier. Second, it is easy to implement. Third, it implicitly includes the effect of finite sample size on the resulting fit uncertainty. Fourth, it includes the effect of fit parameter covariance. The bootstrap method has thus become our error estimation method of choice.

5.1.4. A final note: The residual

It is always worthwhile to plot the difference between the model and the data, known as the residual. A residual with obvious, nonrandom features is a sure sign that the model does not fully capture the data. Furthermore, the features of the residual usually stimulate hypotheses about potential deficiencies in either the data collection methodology or the model. The residual is thus often more helpful in the intermediate stages of data interpretation than numerical goodness-of-fit measures, for example, χ^2.

5.2. Measurement of stroke size: Compliance correction for nonprocessive motors

Accurate and precise measurement of stroke sizes for processive and non-processive motors is complicated by the presence of compliant connections at the bead–actin interface, compliant elements in the myosin and compliance of the myosin to surface attachment (Fig. 14.7). In the case of force-feedback measurements, all of these springs stay stretched to a constant length, and it is therefore possible to measure displacements directly from
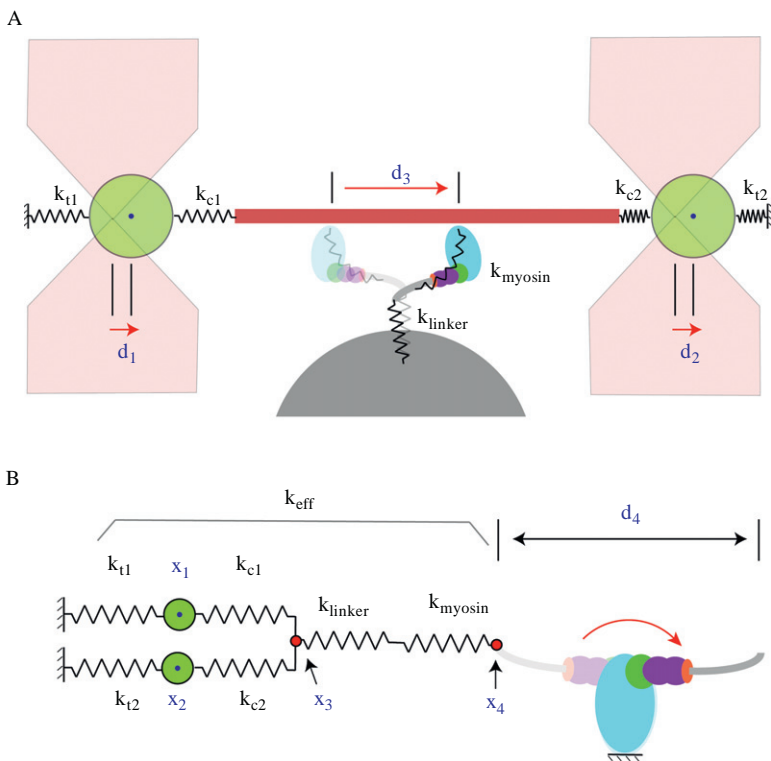
Figure 14.7 Compliance correction in the dual beam optical trap. (A) Cartoon schematic of a myosin in a dual–beam optical trap with compliant elements—a myosin stroke in the presence of compliant elements is depicted. See Fig. 14.1 for the corresponding three-dimensional image. Here, different compliant elements are shown as isotropic linear Hookean springs. The compliant elements include the actin filament to bead connections (k_{c1} and k_{c2}), the $(GSG)_4$ linker (k_{linker}), and the myosin itself (k_{myosin}). In the figure, the stroke displaces the actin filament from left to right, so that the springs on the left side (k_{t1} and k_{c1}) are stretched while those on the right side (k_{t2} and k_{c2}) are compressed. The centers of the trapped beads are indicated by x_1 and x_2. Making a tight dumbbell affects the apparent trap stiffness experienced by the beads. Hence, trap stiffness in the bound state needs to be determined in the compliance correction procedure (see Section 5.2). In the experiment shown in Fig. 14.6, the apparent stroke size before compliance correction is reflected in the displacements d_1 and d_2. The displacement of the position of the myosin–actin binding interface upon going from prestroke to poststroke is d_3. The light and dark myosin images show the prestroke and the poststroke states, respectively. (B) Alternative representation of spring connections in Fig. 14.7A. The springs in Fig. 14.7A can be combined into a serial/parallel combination, such that $k_{eff} = \{(k_{t1}||k_{c1}) + (k_{t2}||k_{c2})\}||(k_{myosin}||k_{linker})$, where $A||B \equiv (A^{-1} + B^{-1})^{-1}$. Despite a change in the position of the second bead, the magnitude and the direction of the force applied by it is the same as in Fig. 14.7A. From the experiment (see first and second graph in Fig. 14.6 as an example), we measure the displacement of the two beads (x_1, x_2). If the spring constant for the compliant elements (k_{c1}, k_{c2}, k_{linker}, and k_{myosin}) are much greater than the trap stiffness (k_{t1}, k_{t2}), the effective stiffness (k_{eff}) can be approximated by $k_{eff} \sim k_{t1} + k_{t2}$. For this case, the bead position displacements (x_1, x_2) reflect the actual stroke size of the myosin (d_4). When the spring constant of the compliant elements is on the order of the trap stiffness, compliance correction is necessary to measure the actual d_4 (compliance correction is explained in Section 5.2).

bead displacements (Visscher *et al.*, 1999). However, stroke-size measurements for nonprocessive motors require compliance correction, especially when the trap stiffness is comparable to or higher than the stiffness of other compliant elements.

5.2.1. Strategy for compliance correction in a dual-beam optical trap

Find interacting platforms with single motors as discussed in Section 4.4. Nonprocessive motors show binding and unbinding events as shown in Fig. 14.6. Binding events result in both a sudden drop in the variance of bead position, as well as in the position correlation between the two beads. These two sources of information, variance and bead–bead correlation, allow us to determine the effective trap stiffness as well as the compliance of individual elements. This technique has been used to measure the stroke contribution of an ER/K α-helix by Sivaramakrishnan *et al.* (2009).

Figure 14.7 is a schematic of the compliant elements in the three-bead assay. Displacement of positions x_1–x_4 is denoted as d_1–d_4. The PSD output directly measures d_1 and d_2 during the experiment. We want to measure the actual myosin stroke size (d_4) in the presence of many compliant elements, such as the actin filament to bead connections (k_{c1} and k_{c2}) and the (GSG)$_4$ linker between the motor and the bead platform (k_{linker}), as well as the flexibility within the myosin (k_{myosin}).

The effective spring constant for the myosin stroke is a mixed serial and parallel combination of each element, expressed as:

$$k_{\text{eff}} = [(k_{t1}||k_{c1}) + (k_{t2}||k_{c2})]||(k_{\text{myosin}}||k_{\text{linker}}), \qquad (14.11)$$

where $A||B \equiv (A^{-1} + B^{-1})^{-1}$. Here, k_{t1} and k_{t2} are the trap stiffnesses after making a tight dumbbell. Since the formation of the tight dumbbell displaces the trapped beads from the center of the trapping beam, k_{t1} and k_{t2} are usually higher than those for the trapped beads in the absence of a dumbbell ($\sim 10\%$ greater by experience). To simplify the mathematical expression, we define ($k_c = k_{c1} || k_{c2}$) for the serial connection of the actin filament to bead connections, and ($k_{\text{xb}} = k_{\text{myosin}} || k_{\text{linker}}$) for the stiffness of the cross-bridge, which is a serial combination of the myosin and the flexible linker. Simple algebra allows us to derive the diffusion correlation coefficient of the two beads (CorrCoef, see Section A.2) as a function of (k_{t1}, k_{t2}, k_{c1}, k_{c2}, k_{xb}), as first outlined by Mehta *et al.* (1997). This method is subsequently described in detail. Additionally, we measure the effective spring constant of each bead with the dumbbell present, in both the bound (k_{b1}, k_{b2}) and unbound (k_{u1}, k_{u2}) states. This information is essential to calculate the different compliances.

Step 1 In the unbound state, determine k_{t1}, k_{t2}, and k_c from the measured k_{u1}, k_{u2}, and CorrCoef

We determine the effective trap stiffnesses (k_{t1} and k_{t2}) and the bead–actin connection stiffness (k_c), in the presence of a tight dumbbell, from a combination of analytical expressions and numerical computation.

(a) Select initial values for k_{t1} and k_{t2}. We use values from the calibration of trap stiffnesses without the dumbbell.
(b) Obtain k_c using *CorrCoef* with a given k_{t1} and k_{t2}. We assume $k_{xb} = 0$ (no myosin attachment), and $k_{c1} = k_{c2} = 2k_c$.
(c) Given k_c and the measured k_{u1} and k_{u2}, we can analytically determine the new k_{t1} and k_{t2}:

$$k_{u1} = k_{t1} + (k_{t2} || k_c), \tag{14.12}$$

$$k_{u2} = k_{t2} + (k_{t1} || k_c). \tag{14.13}$$

(d) Iterate (b) and (c) until k_{t1}, k_{t2}, and k_c converge. We observe good convergence after a few rounds of iteration.

Step 2 Determine k_{c1} and k_{c2}

We determine k_{c1} and k_{c2} analytically, using the following two expressions, with values for k_{t1}, k_{t2}, and k_c obtained from Step 1, and the measured displacement during the binding event of the first bead (d_1) and the second bead (d_2):

$$k_c = k_{c1} || k_{c2}, \tag{14.14}$$

$$d_3 = d_1 \frac{k_{t1} + k_{c1}}{k_{c1}} = d_2 \frac{k_{t2} + k_{c2}}{k_{c2}}. \tag{14.15}$$

Thus, we now know the values of k_{t1}, k_{t2}, k_{c1}, and k_{c2}.

Step 3 Determine k_{xb}

We next use the CorrCoef function to fit the data collected during the binding events. We already know four variables of this function, namely k_{t1}, k_{t2}, k_{c1}, and k_{c2}, so we can determine the last unknown k_{xb}.

Step 4 Determine the stroke size of the motor (d_4) from previously determined values for k_{t1}, k_{t2}, k_{c1}, k_{c2}, and k_{xb}

The stroke size of myosin in the presence of compliant elements is given by:

$$d_4 = d_3 \frac{k_{tc} + k_{xb}}{k_{xb}}, \qquad (14.16)$$

where $k_{tc} = (k_{t1}||k_{c1}) + (k_{t2}||k_{c2})$.

6. Conclusion

This chapter has detailed the assembly of a modern dual–beam optical trap, described the experimental protocols involved in analyzing molecular motors using the trap, and provided methods of analysis often missing in similar publications. Even the novice should find it possible to set up the trap and carry out appropriate experiments using this chapter as a guide. We hope we have at least partially achieved our aim.

Appendix

A.1. Alignment for the feedback control of a single beam by the AOD

The dual-beam optical trap setup in Fig. 14.2 is a design optimized for the three-bead assay. However, some dual-beam experiments require feedback control of only one beam. Here, we introduce a simple modification of the current design for the single-beam feedback control. We now use the s-polarized component of PBS1, which is beam-blocked in Fig. 14.2, panel 1. Move BD 5 in. away from PBS such that BD is placed to the left of the beam path from AOD to L1. Insert another PBS (PBS7) between AOD and L1 such that the s-polarized beam from PBS1 is directed to L1. Beam coupling can be done by iteratively adjusting the angle of PBS1 and PBS7. Move the position of HP2 between PBS1 and PBS7. By rotating the angle of HP2, the power of the s-polarized beam can be adjusted and directed to L1. The p-polarized component is passing through the AOD and therefore can be feedback controlled, whereas the s-polarized beam is not controlled by the AOD. In addition, the p- and s-polarized beams are reflected on PM1 and PM2, respectively, so that both of them can be coarsely positioned as described earlier.

A.2. Correlation coefficient between two trapped beads (CorrCoef)

In the three-bead assay, two trapped beads are connected with each other by a tight actin dumbbell. Therefore, the position of each bead in the diffusive motion is correlated with a finite correlation coefficient. We use the diffusion correlation coefficient between two trapped beads to characterize the compliant elements as described in Section 5.2. This method was derived by Mehta *et al.* (1997), and here we show the explicit form of the correlation coefficient function (CorrCoef).

Consider the situation in which two beads are connected to each other through the actin dumbbell and the dumbbell interacts with a motor as depicted in Fig. 14.7A. In this heavily overdamped environment (low Reynolds number), the Langevian equations for the two beads are expressed as

$$F_1(t) - k_{t1}x_1(t) - \gamma\frac{dx_1(t)}{dt} + k_{c1}[x_3(t) - x_1(t)] = 0, \quad (14.A1)$$

$$F_2(t) - k_{t2}x_2(t) - \gamma\frac{dx_2(t)}{dt} + k_{c2}[x_3(t) - x_2(t)] = 0, \quad (14.A2)$$

where $\gamma = 6\pi\eta r$, η is the viscosity of the liquid, and r is the radius of the beads. Note that this description of γ is only strictly true for a sphere far from the coverslip surface. More accurate treatments based on Faxen's law for describing the drag on a sphere near a surface are detailed elsewhere (Neuman and Block, 2004). The four terms in Eqs. (14.A1) and (14.A2) refer to the thermal force, trapping force, drag force, and the force from actin dumbbell, respectively. At any time t, as per Newton's second law, the forces on the actin filament must sum to zero. The equation of motion at x_3 is:

$$k_{c1}[x_1(t) - x_3(t)] + k_{c2}[x_2(t) - x_3(t)] - k_{xb}x_3(t) = 0, \quad (14.A3)$$

where k_{xb} refers to the spring constant for the cross-bridge that is the serial combination of the myosin and anchoring linker on the surface. For example, $k_{xb} = 0$ represents the unbound state, whereas $k_{xb} \to \infty$ indicates the bound state with infinite stiffness of the connection. Solving the three Eqs. (14.A1)–(14.A3), we get

$$\begin{aligned}F_1(t) &- \left[k_{t1} + \frac{k_{c1}(k_{c2} + k_{xb})}{k_{c1} + k_{c2} + k_{xb}}\right]x_1(t) - \gamma\frac{dx_1(t)}{dt} \\ &+ \left[\frac{k_{c1}k_{c2}}{k_{c1} + k_{c2} + k_{xb}}\right]x_2(t) = 0,\end{aligned} \quad (14.A4)$$

$$F_2(t) - \left[k_{t2} + \frac{k_{c2}(k_{c1} + k_{xb})}{k_{c1} + k_{c2} + k_{xb}} \right] x_2(t) - \gamma \frac{dx_2(t)}{dt}$$
$$+ \left[\frac{k_{c1}k_{c2}}{k_{c1} + k_{c2} + k_{xb}} \right] x_1(t) = 0. \tag{14.A5}$$

Now, we Fourier transform and obtain

$$X_1(f) = \frac{A F_1(f) + C F_2(f)}{A B - C^2}, \tag{14.A6}$$

$$X_2(f) = \frac{B F_2(f) + C F_1(f)}{A B - C^2}, \tag{14.A7}$$

where $A = k_{t2} + \frac{k_{c2}(k_{c1}+k_{xb})}{k_{c1}+k_{c2}+k_{xb}} + i2\pi f\gamma$, $\quad B = k_{t1} + \frac{k_{c1}(k_{c2}+k_{xb})}{k_{c1}+k_{c2}+k_{xb}} + i2\pi f\gamma$, $C = \frac{k_{c1}k_{c2}}{k_{c1}+k_{c2}+k_{xb}}$.

Since we are collecting data in a finite measurement time ($T_{msr} = 1/f_{msr}$) with a finite sampling rate ($f_{sampling} = 10\,kHz$), the set of frequency range is given by $f = f_{msr} \times k$, where $k = [1, 2, \ldots K, N]$ with total sampling number N. Now, we want to calculate the correlation coefficient between two sampled signals $x_1(n)$ and $x_2(n)$ whose discrete Fourier transforms are $X_1(k)$ and $X_2(k)$. Using Parseval's theorem, the correlation coefficient between the two beads is

$$\text{CorrCoef} = \frac{\sum[x_1(n)x_2(n)]}{\sqrt{\sum[x_1(n)]^2 \sum[x_2(n)]^2}} = \frac{\sum[X_1(k)X_2^*(k)]}{\sqrt{\sum[X_1(k)]^2 \sum[X_2(k)]^2}}. \tag{14.A8}$$

The thermal forces working on the two beads cannot be correlated with each other, so the cross-term can be dropped as

$$\sum F_1(k) F_2(k) = 0.$$

We assume that $F_1(n)$ and $F_2(n)$ at every frequency are identical on average, since their time scales are much faster than any other related time scales. Thus, we cancel out $|F_1|^2$ and $|F_2|^2$ in the numerator and the denominator in Eq. (14.A8). Therefore, the final expression for the correlation coefficient is

$$\text{CorrCoef} = \frac{\sum \frac{AC^* + B^*C}{|AB - C^2|^2}}{\sqrt{\left[\sum \frac{AA^* + CC^*}{|AB - C^2|^2}\right]\left[\sum \frac{BB^* + CC^*}{|AB - C^2|^2}\right]}}. \qquad (14.A9)$$

Since CorrCoef is a function of $[k_{t1}, k_{t2}, k_{c1}, k_{c2}, k_{xb}]$ and also a measurable quantity in our experiment, we can determine one unknown given four other quantities.

ACKNOWLEDGMENTS

REFERENCES

Ashkin, A. (1992). Forces of a single-beam gradient laser trap on a dielectric sphere in the ray optics regime. *Biophys. J.* **61,** 569–582.

Berg-Sørensen, K., and Flyvbjerg, H. (2004). Power spectrum analysis for optical tweezers. *Rev. Sci. Instrum.* **75,** 594–612.

Block, S. M. (1998). Construction of optical tweezers. *In* ''Cells: A Laboratory Manual,'' (D. Spector, R. Goldman, and L. Leinwand, eds.), Cold Spring Harbor Laboratory Press, New York.

Bryant, Z., Altman, D., and Spudich, J. A. (2007). The power stroke of myosin VI and the basis of reverse directionality. *Proc. Natl. Acad. Sci. USA* **104,** 772–777.

Bustamante, C., Chemla, Y. R., and Moffitt, J. R. (2007). High-resolution dual-trap optical tweezers with differential detection. *In* ''Single-Molecule Techniques: A Laboratory Manual,'' (P. R. Selvin and T. Ha, eds.), pp. 297–324. Cold Spring Harbor Laboratory Press, New York.

Carter, A. R., Seol, Y., and Perkins, T. T. (2009). Precision surface-coupled optical-trapping assay with one-basepair resolution. *Biophys. J.* **96,** 2926–2934.

Churchman, L. S., Okten, Z., Rock, R. S., Dawson, J. F., and Spudich, J. A. (2005). Single molecule high-resolution colocalization of Cy3 and Cy5 attached to macromolecules measures intramolecular distances through time. *Proc. Natl. Acad. Sci. USA* **102,** 1419–1423.

Dominguez, R., Freyzon, Y., Trybus, K. M., and Cohen, C. (1998). Crystal structure of a vertebrate smooth muscle myosin motor domain and its complex with the essential light chain: Visualization of the pre-power stroke state. *Cell* **94,** 559–571.

Dunn, A. R., and Spudich, J. A. (2007). Dynamics of the unbound head during myosin V processive translocation. *Nat. Struct. Mol. Biol.* **14,** 246–248.

Efron, B., and Tibshirani, R. J. (1994). An Introduction to the Bootstrap. Chapman & Hall, New York.

Finer, J. T., Simmons, R. M., and Spudich, J. A. (1994). Single myosin molecule mechanics: Piconewton forces and nanometre steps. *Nature* **368,** 113–119.

Gittes, F., and Schmidt, C. F. (1998a). Interference model for back-focal-plane displacement detection in optical tweezers. *Opt. Lett.* **23,** 7–9.

Gittes, F., and Schmidt, C. F. (1998b). Signals and noise in micromechanical measurements. *Method Cell Biol.* **55,** 129–156.

Guilford, W. H., Dupuis, D. E., Kennedy, G., Wu, J., Patlak, J. B., and Warshaw, D. M. (1997). Smooth muscle and skeletal muscle myosins produce similar unitary forces and displacements in the laser trap. *Biophys. J.* **72,** 1006–1021.

Harada, Y., Noguchi, A., Kishino, A., and Yanagida, T. (1987). Sliding movement of single actin filaments on one-headed myosin filaments. *Nature* **326,** 805–808.

Hohng, S., Zhou, R., Nahas, M. K., Yu, J., Schulten, K., Lilley, D. M., and Ha, T. (2007). Fluorescence-force spectroscopy maps two-dimensional reaction landscape of the holliday junction. *Science* **318,** 279–283.

Huisstede, J. H. G., van Rooijen, B. D., van der Werf, K. O., Bennink, M. L., and Subramaniam, V. (2006). Dependence of silicon position-detector bandwidth on wavelength, power, and bias. *Opt. Lett.* **31,** 610–612.

Huxley, H. E. (1969). The mechanism of muscular contraction. *Science* **164,** 1356–1365.

Ishijima, A., Kojima, H., Funatsu, T., Tokunaga, M., Higuchi, H., Tanaka, H., and Yanagida, T. (1998). Simultaneous observation of individual ATPase and mechanical events by a single myosin molecule during interaction with actin. *Cell* **92,** 161–171.

Kad, N. M., Trybus, K. M., and Warshaw, D. M. (2008). Load and Pi control flux through the branched kinetic cycle of myosin V. *J. Biol. Chem.* **283,** 17477–17484.

Kron, S. J., and Spudich, J. A. (1986). Fluorescent actin filaments move on myosin fixed to a glass surface. *Proc. Natl. Acad. Sci. USA* **83,** 6272–6276.

Laakso, J. M., Lewis, J. H., Shuman, H., and Ostap, E. M. (2008). Myosin I can act as a molecular force sensor. *Science* **321,** 133–136.

Lang, M. J., Asbury, C. L., Shaevitz, J. W., and Block, S. M. (2002). An automated two-dimensional optical force clamp for single molecule studies. *Biophys. J.* **83,** 491–501.

Lang, M. J., Fordyce, P. M., Engh, A. M., Neuman, K. C., and Block, S. M. (2004). Simultaneous, coincident optical trapping and single-molecule fluorescence. *Nat. Methods* **1,** 133–139.

Lee, W. M., Reece, P. J., Marchington, R. F., Metzger, N. K., and Dholakia, K. (2007). Construction and calibration of an optical trap on a fluorescence optical microscope. *Nat. Protoc.* **2,** 3226–3238.

Marston, S. B., and Taylor, E. W. (1980). Comparison of the myosin and actomyosin ATPase mechanisms of the four types of vertebrate muscles. *J. Mol. Biol.* **139,** 573–600.

Mehta, A. D., Finer, J. T., and Spudich, J. A. (1997). Detection of single-molecule interactions using correlated thermal diffusion. *Proc. Natl. Acad. Sci. USA* **94,** 7927–7931.

Mehta, A. D., Rock, R. S., Rief, M., Spudich, J. A., Mooseker, M. S., and Cheney, R. E. (1999). Myosin-V is a processive actin-based motor. *Nature* **400,** 590–593.

Moffitt, J. R., Chemla, Y. R., Izhaky, D., and Bustamante, C. (2006). Differential detection of dual traps improves the spatial resolution of optical tweezers. *Proc. Natl. Acad. Sci. USA* **103,** 9006–9011.

Moffitt, J. R., Chemla, Y. R., Smith, S. B., and Bustamante, C. (2008). Recent advances in optical tweezers. *Annu. Rev. Biochem.* **77,** 205–228.

Molloy, J. E., Burns, J. E., Kendrick-Jones, J., Tregear, R. T., and White, D. C. (1995). Movement and force produced by a single myosin head. *Nature* **378,** 209–212.

Neuman, K. C., and Block, S. M. (2004). Optical trapping. *Rev. Sci. Instrum.* **75,** 2787–2809.

Nishikawa, S., Komori, T., Ariga, T., Okada, T., Morimatsu, M., Ishii, Y., and Yanagida, T. (2007). Imaging and nanomanipulation of an actomyosin motor. *In* "Single-Molecule Techniques: A Laboratory Manual," (P. R. Selvin and T. Ha, eds.), pp. 325–346. Cold Spring Harbor Laboratory Press, New York.

Nugent-Glandorf, L., and Perkins, T. T. (2004). Measuring 0.1-nm motion in 1 ms in an optical microscope with differential back-focal-plane detection. *Opt. Lett.* **29,** 2611–2613.

Palmiter, K. A., Tyska, M. J., Dupuis, D. E., Alpert, N. R., and Warshaw, D. M. (1999). Kinetic differences at the single molecule level account for the functional diversity of rabbit cardiac myosin isoforms. *J. Physiol.* **519**(Pt 3), 669–678.

Palmiter, K. A., Tyska, M. J., Haeberle, J. R., Alpert, N. R., Fananapazir, L., and Warshaw, D. M. (2000). R403Q and L908V mutant beta-cardiac myosin from patients with familial hypertrophic cardiomyopathy exhibit enhanced mechanical performance at the single molecule level. *J. Muscle Res. Cell Motil.* **21,** 609–620.

Perkins, T. T. (2009). Optical traps for single molecule biophysics: A primer. *Laser & Photon. Rev.* **3,** 203–220.

Peterman, E. J. G., Gittes, F., and Schmidt, C. F. (2003). Laser-induced heating in optical traps. *Biophys. J.* **84,** 1308–1316.

Pralle, A., Prummer, M., Florin, E. L., Stelzer, E. H., and Horber, J. K. (1999). Three-dimensional high-resolution particle tracking for optical tweezers by forward scattered light. *Microsc. Res. Tech.* **44,** 378–386.

Purcell, T. J., Morris, C., Spudich, J. A., and Sweeney, H. L. (2002). Role of the lever arm in the processive stepping of myosin V. *Proc. Natl. Acad. Sci. USA* **99,** 14159–14164.

Purcell, T. J., Sweeney, H. L., and Spudich, J. A. (2005). A force-dependent state controls the coordination of processive myosin V. *Proc. Natl. Acad. Sci. USA* **102,** 13873–13878.

Rao, C. R. (1965). Linear Statistical Inference and Its Application. John Wiley & Sons, Inc., New York.

Rayment, I., Rypniewski, W. R., Schmidt-Base, K., Smith, R., Tomchick, D. R., Benning, M. M., Winkelmann, D. A., Wesenberg, G., and Holden, H. M. (1993). Three-dimensional structure of myosin subfragment-1: A molecular motor. *Science* **261,** 50–58.

Rice, S. E., Purcell, T. J., and Spudich, J. A. (2003). Building and using optical traps to study properties of molecular motors. *Methods Enzymol.* **361,** 112–133.

Rief, M., Rock, R. S., Mehta, A. D., Mooseker, M. S., Cheney, R. E., and Spudich, J. A. (2000). Myosin-V stepping kinetics: A molecular model for processivity. *Proc. Natl. Acad. Sci. USA* **97,** 9482–9486.

Rock, R. S., Rice, S. E., Wells, A. L., Purcell, T. J., Spudich, J. A., and Sweeney, H. L. (2001). Myosin VI is a processive motor with a large step size. *Proc. Natl. Acad. Sci. USA* **98,** 13655–13659.

Sakamoto, T., Webb, M. R., Forgacs, E., White, H. D., and Sellers, J. R. (2008). Direct observation of the mechanochemical coupling in myosin Va during processive movement. *Nature* **455,** 128–132.

Simmons, R. M., Finer, J. T., Chu, S., and Spudich, J. A. (1996). Quantitative measurements of force and displacement using an optical trap. *Biophys. J.* **70,** 1813–1822.

Sivaramakrishnan, S., Spink, B. J., Sim, A. Y., Doniach, S., and Spudich, J. A. (2008). Dynamic charge interactions create surprising rigidity in the ER/K alpha-helical protein motif. *Proc. Natl. Acad. Sci. USA* **105,** 13356–13361.

Sivaramakrishnan, S., Sung, J., Ali, M., Doniach, S., Flyvbjerg, H., and Spudich, J. A. (2009). Combining single molecule optical trapping and small angle X-ray scattering measurements to compute the persistence length of a protein ER/K alpha-helix. *Biophys. J.* **97,** 2993–2999.

Spudich, J. A. (2001). The myosin swinging cross-bridge model. *Nat. Rev. Mol. Cell Biol.* **2,** 387–392.

Spudich, J. A., and Sivaramakrishnan, S. (2009). Myosin VI: An innovative motor that challenged the swinging lever arm hypothesis. *Nat. Rev. Mol. Cell Biol.* **11,** 128–137.

Spudich, J. A., Rice, S. E., Rock, R. S., Purcell, T. J., and Warrick, H. M. (2007). Optical traps to study properties of molecular motors. *In* "Single-Molecule Techniques: A Laboratory Manual," (P. R. Selvin and T. Ha, eds.), pp. 279–296. Cold Spring Harbor Laboratory Press, New York.

Svoboda, K., and Block, S. M. (1994). Biological applications of optical forces. *Annu. Rev. Biophys. Biomol. Struct*. **23**, 247–285.

Tolic–Norrelykke, I. M., Berg–Sørensen, K., and Flyvbjerg, H. (2004). MatLab program for precision calibration of optical tweezers. *Comput. Phys. Comm*. **159**, 225–240.

Tolic–Norrelykke, S. F., Schaeffer, E., Howard, J., Pavone, F. S., Juelicher, F., and Flyvbjerg, H. (2006). Calibration of optical tweezers with positional detection in the back–focal–plane. *Rev. Sci. Instrum*. **77**, 103101.

Uyeda, T. Q., Kron, S. J., and Spudich, J. A. (1990). Myosin step size. Estimation from slow sliding movement of actin over low densities of heavy meromyosin. *J. Mol. Biol*. **214**, 699–710.

van Dijk, M. A., Kapitein, L. C., van Mameren, J., Schmidt, C. F., and Peterman, E. J. G. (2004). Combining optical trapping and single-molecule fluorescence spectroscopy: Enhanced photobleaching of fluorophores. *J. Phys. Chem. B* **108**, 6479–6484.

Veigel, C., Coluccio, L. M., Jontes, J. D., Sparrow, J. C., Milligan, R. A., and Molloy, J. E. (1999). The motor protein myosin-I produces its working stroke in two steps. *Nature* **398**, 530–533.

Veigel, C., Wang, F., Bartoo, M. L., Sellers, J. R., and Molloy, J. E. (2002). The gated gait of the processive molecular motor, myosin V. *Nat. Cell Biol*. **4**, 59–65.

Veigel, C., Schmitz, S., Wang, F., and Sellers, J. R. (2005). Load-dependent kinetics of myosin-V can explain its high processivity. *Nat. Cell Biol*. **7**, 861–869.

Visscher, K., and Block, S. M. (1998). Versatile optical traps with feedback control. *Methods Enzymol*. **298**, 460–489.

Visscher, K., Gross, S. P., and Block, S. M. (1996). Construction of multiple-beam optical traps with nanometer-resolution position sensing. *IEEE J. Sel. Top. Quantum Electron*. **2**, 1066–1076.

Visscher, K., Schnitzer, M. J., and Block, S. M. (1999). Single kinesin molecules studied with a molecular force clamp. *Nature* **400**, 184–189.